DOE/NASA/0006-1
NASA CR-165209

DETERMINATION OF HYDROGEN PERMEABILITY IN UNCOATED AND COATED SUPERALLOYS INTERIM REPORT

S. Bhattacharyya, E. J. Vesely, Jr., and V. L. Hill
IIT Research Institute
10 West 35th Street
Chicago, Illinois 60616

JANUARY 1981

Prepared for
NATIONAL AERONAUTICS AND SPACE ADMINISTRATION
Lewis Research Center
Under Contract DEN 3-6

for
U.S. DEPARTMENT OF ENERGY
Office of Transportation Programs

DOE/NASA/0006-1
NASA CR-165209

DETERMINATION OF HYDROGEN PERMEABILITY IN UNCOATED AND COATED SUPERALLOYS INTERIM REPORT

S. Bhattacharyya, E. J. Vesely, Jr., and V. L. Hill
IIT Research Institute
10 West 35 Street
Chicago, Illinois 60616

January 1981

Prepared for
NATIONAL AERONAUTICS AND SPACE ADMINISTRATION
Lewis Research Center
Under Contract DEN3-6

for
U.S. DEPARTMENT OF ENERGY
Office of Transportation Programs
Under Interagency Agreement DE-A-101-77CS51040

TABLE OF CONTENTS

LIST OF TABLES

LIST OF FIGURES

LIST OF FIGURES (cont.)

SUMMARY

This report, NASA CR-165209, under Contract DEN3-6 summarizes the results of hydrogen permeability, diffusivity, and solubility measurements for seven iron-base alloys and one cobalt-base alloy over the range 650°-815°C (1200°-1500°F). The test alloys included wrought iron-base alloys Multimet N-155, Incoloy 800, A-286, and 19-9DL, and cast alloys XF-818, SAF-11, and CRM-6D. The cobalt-base alloy was low carbon 6B. In addition to permeability for uncoated alloys, the effects of four selected coatings were assessed on Multimet N-155, and the best coating was applied to the other wrought iron-base alloys. Apparent activation energies for permeability and diffusivity were calculated from Arrhenius plots of the data.

INTRODUCTION

The Stirling engine currently under development by the Department of Energy employs hydrogen as the working fluid. Containment of hydrogen under the high operating temperatures and pressures of the engine is a major technical problem. Few data[1-4] exist on the rate of permeation of hydrogen through iron-base and other high-temperature alloys at high temperatures and pressures. Furthermore, the long-term effects of hydrogen on the physical and mechanical properties are also unknown. For these reasons, evaluation of candidate alloys for the heater head and heat exchanger tubing of the Stirling Engine is in progress. This report summarizes the initial work on measurement of hydrogen permeability in several candidate alloys.

This report, NASA CR-165209, under Contract DEN3-6, contains hydrogen permeability, diffusivity, and solubility data for seven iron-base alloys and one cobalt-base alloy measured over the range 650°-815°C (1200°-1500°F). The iron-base alloys included IN 800, 19-9DL, Multimet N-155, A-286, CRM-6D, SAF-11, XF-818, and the cobalt-base alloy was low carbon 6B. Also included in this report are permeability measurements on iron-base alloys coated with commercially available coatings. These included Al_2O_3, glass, silicon nitride, and aluminide diffusion coatings applied on N-155, and an aluminide diffusion coating on 19-9DL, A-286, and IN 800.

Permeability testing was conducted in a test facility designed and constructed by IITRI prior to the start of the test program. This facility was designed to operate at pressures up to 20.7 MPa (3000 psi) and temperatures to 1200°C. Permeability measurements in this program, however, were limited to 20.7 MPa and 815°C.

DETERMINATION OF PERMEABILITY

Background

Any component containing hydrogen heated to high temperature will suffer loss of hydrogen through the container walls by permeation. The rate of hydrogen loss per unit area will be dependent on the temperature and pressure of the system and the construction materials of the component. Theoretically, wall thickness of the container is not a variable since increasing wall thickness serves merely to delay the appearance of hydrogen on the external surface. Because of this, specimen thickness was not variable and all permeability measurements were made on 0.64 cm (0.25 in.) thick specimens.

Classically, permeation of any diatomic gas such as hydrogen through a solid, isotropic material involves several major steps constituting the permeation process:

1) Adsorption of the gas molecules on the surface

2) Dissociation of diatomic molecules into atomic species

3) Diffusion of the dissociated atoms through the solid

4) Recombination of atomic species to diatomic species at the external surface

5) Desorption from the surface.

For any diatomic gas, the slowest of the above steps, at the pressure and temperature of the system, controls the permeation rate. At low temperatures, step 2 may control the overall permeation rate. However, at the high temperatures employed in this program, it is most probable that diffusion through the metal controls the process. This was assumed in conduct of the permeability measurements in this program.

The high velocity of H_2-metal diffusion is generally associated with the interstitial solution of these gases in metals. It is to be expected, therefore, that the activation energy of gas-metal diffusion should be much less than that for most metal-metal processes. In general, the activation energy falls in the range of 5 to 20 kcal/g-atom,[3] but the available data are difficult to interpret because of the several steps of the permeation process and their associated energies.

If diffusion is the rate-controlling step, then the flow of gaseous molecules can be expressed by

$$j_t = \phi \frac{A}{\Delta x} (p_i^{\frac{1}{2}} - p_o^{\frac{1}{2}}) \qquad (1)$$

where j_t = hydrogen flux normal to the surface of the membrane (specimen), $cm^3\ s^{-1}$ (STP)

ϕ = permeability, $cm^3\ s^{-1} cm^{-1} MPa^{-\frac{1}{2}}$

A = membrane area, cm^2

Δx = membrane thickness, cm

p_i = input pressure, MPa

p_o = output pressure, MPa.

The flux normal to the surface obeys Fick's first law

$$J = -D\frac{dc}{dx} \tag{2}$$

and, under steady-state permeation conditions, dc/dx will be constant. Integrating Equation 2 for a disk of area A and thickness Δx provides

$$j_t = -\frac{DA}{\Delta x}(C_o - C_i) \tag{3}$$

where C_o and C_i are the solute concentrations at the output and input surfaces, respectively.

When diffusion is the rate-controlling step, C_o and C_i are given by Sievert's Law. For monatomic gas in a metal, assuming ideal behavior:

$$C = KP^{\frac{1}{2}} \tag{4}$$

where C = solute concentration

K = solubility constant

P = external pressure.

Substituting this in Equation 3 gives

$$j_t = \frac{-DAK}{\Delta x}(p_o^{\frac{1}{2}} - p_i^{\frac{1}{2}}) \tag{5}$$

Thus, from Equations 1 and 5 with the implied assumptions,

$$\emptyset = DK \tag{6}$$

The diffusion term, D, and the solubility term, K, may be assumed to vary with temperature according to the Arrhenius-type equations:

$$D = D_o \exp^{-E_a/RT} \tag{7}$$

$$K = K_o \exp^{-\Delta H_s/RT} \tag{8}$$

where E_a is activation energy for self-diffusion and ΔH_s is the heat of solution.

The variation of permeability with temperature may therefore follow an equation of the type:

$$\phi = \phi_o \exp^{-\Delta H_p/RT} \tag{9}$$

where $\phi_o = D_o K_o$

$\Delta H_p = E_a + \Delta H_s$.

If the output pressure is very much less than the inlet pressure such that $p_o^{\frac{1}{2}}$ is negligible--for example, when the inlet pressure was 20.7 MPa and the outlet pressure was less than atmospheric as in this program:

$$j_t = \frac{A p_i^{\frac{1}{2}}}{\Delta x} \cdot K_o \exp^{-\Delta H_s/RT} \cdot D_o \exp^{-E_a/RT} \tag{10}$$

Thus, for conditions of diffusion control,

$$j_t \propto p^{\frac{1}{2}} \tag{11}$$

$$\ln j_t \propto -\frac{1}{T} \tag{12}$$

$$j_t \propto \frac{1}{\Delta x} \tag{13}$$

In order to determine the value of D from permeation data, hydrogen diffusion must be rate controlling. If the above three conditions are met, the solubility constant can be estimated from permeability if the diffusion term is known and the relative values are significantly different.

Clearly, the above analysis depends on the membrane being an isotropic material without allotropic and structural changes in the crystal structure within the temperature range of interest. Furthermore, chemical reactions must not occur between the diffusing atoms and the membrane constituents. In real systems such as superalloys, these ideal conditions probably do not prevail fully. For example, though H_2 diffusion in iron is endothermic, reaction with carbon in the alloys to produce methane is known to occur. The degree of cold working has been shown to be significant in a large number of alloys. Furthermore, the presence of porosity and precipitates in these alloys may also influence diffusivity, hence permeability and solubility, in the alloy matrix. Finally, time-dependent microstructural changes such as void formation will likely modify permeability rates. All of these factors indicate that permeability data obtained in this program must be classified as a semiquantitative comparison

of hydrogen permeability for the alloys investigated in this program and information obtained through derivation from the primary, measured data should be used carefully.

Experimental Determination of Permeability

Experimentally, both permeability (Ø) and diffusivity (D) can be determined by measurement, in units convertible to mass, of the amount of hydrogen emerging from the output surface of the membrane. Clearly, there will be a finite interval between the time that the hydrogen gas is permitted to contact the input surface until it emerges at a constant rate from the exit side. Accordingly, a plot of an experimentally measured quantity of hydrogen emerging from the exit side will have the shape shown in Fig. 1. For permeability measurements, the quantity of gas emerging is usually measured by either volume or pressure changes.

For volume methods at constant pressure,

$$j_t = K\frac{dv}{dt} \tag{14}$$

where K = a constant of the experimental apparatus.

For pressure change methods at constant volume,

$$j_t = \frac{V_o}{RT_i}\frac{dP}{dt} \tag{15}$$

where T_i = temperature of the output volume, V_o

R = gas constant.

The pressure change method was used in the program for permeability measurements. Other experimentally determinable parameters necessary for permeability calculations from Equation 1 were:

1) Membrane thickness (Δx): 0.64 cm (0.250 in.)

2) Input pressure (p_i): 20.7 MPa (3000 psi)

3) Membrane temperature (T_i): 650°-815°C (1200°-1500°F)

The steady-state slope (α) of the output side volume (converted to pressure) versus time curve in Fig. 1 was used to calculate hydrogen flux, j_t, and the intercept on the time axis, Θ_L, is

lag time. Permeability, $\emptyset$, was calculated using Equations 15 and 1 with known input data. The diffusion term was then calculated from the lag time, θ_L, as described below.

Barrer[5,6] has shown mathematically that, for a disk-shaped membrane, D is related to θ_L according to the equation:

$$\theta_L = \frac{(\Delta x)^2}{6D} \cdot \frac{(C_2 + 2C_1 - 3C_0)}{(C_2 - C_1)} \qquad (16)$$

where C_2 = solute concentration at the input surface

C_1 = solute concentration at the output surface

C_0 = initial solute concentration within the membrane.

Since the specimen was degassed under vacuum before hydrogen was introduced at the input side and a vacuum maintained on the output side, $C_1 = C_0$, and

$$\theta_L = \frac{(\Delta x)^2}{6D} \qquad (17)$$

Accordingly, by continually monitoring the pressure of hydrogen emerging from the output surface with time, the steady-state hydrogen flux, j_t, and the lag time, θ_L, were obtained experimentally. The permeability and diffusion terms were calculated from these experimental data and the solubility constants estimated from Equation 6.

Using values of permeability ($\emptyset$) and diffusivity (D) at different temperatures, Arrhenius plots were made from which $\emptyset_o$ and D_o, as well as their respective activation energies were obtained.

MATERIALS AND EXPERIMENTAL PROCEDURE

Test Materials and Specimen Configuration

This program involved measurement of permeabilities and diffusivities for seven uncoated iron-base alloys and one cobalt-base alloy. From these measurements, solubility values were derived.

In addition to the eight uncoated alloys, four commercial coatings applied to the iron-base alloys were investigated for effectiveness in reducing hydrogen permeation. The seven iron-base alloys included wrought alloys Multimet N-155, Incoloy 800

(IN 800), A-286, 19-9DL, and cast alloys CRM-6D, SAF-11, and XF-818. Low carbon alloy 6B, a cobalt-base alloy was also investigated. Chemical compositions of the alloys are listed in Table 1. Heat treatments given to N-155, IN 800, A-286, and 19-9DL are also included in Table 1.

The four coatings evaluated included high-density alumina, silicon nitride, fused glass, and pack diffusion aluminide. All coatings were applied by the coating manufacturers on specimens supplied by IITRI. Specifications for the coatings are listed in Table 2. Appearance of typical uncoated and coated specimens is shown in Fig. 2.

Initially, the effects of all four coatings on hydrogen permeability were evaluated on N-155 over the range 650°-815°C. Subsequently, the best performing coatings, HWS 25000 (aluminide), was applied to IN 800, A-286, and 19-9DL for permeability measurements over the same temperature range.

Wrought test specimens, 6.35 cm diameter and 0.64 cm thick with a circular area 1 cm in diameter, were used. Subsequently, the overall sample size was reduced to 4.74 cm diameter for the cast alloys because of limitation in material availability. Samples as small as 3.02 cm were employed in later tests. In all cases, the effective area exposed to hydrogen was 0.785 cm^2.

On receipt of the test material, the alloys were stamped into disks which were then surface ground parallel to 0.64 cm thickness. Cast specimens were checked for surface cracks or porosity by dye penetrant inspection. After surface grinding, sealing grooves were machined into the surface as shown in Fig. 3. Coated specimens had sealing grooves on one surface only (Fig. 3a), whereas uncoated samples had top and bottom grooves as shown in Fig. 3b. It was necessary to employ graphite gaskets for the coated samples to avoid fracture of the coating during testing.

Sealing was a major problem in initial permeability tests. It was found by experimentation that the mismatched angle seal design shown in Fig. 4 was effective in reducing nitrogen leaks to an acceptable level for permeability measurements. This design consisted of a 70° angle for the head projection and a 60° angle in the specimen seal groove. Low leak rates were obtained by preloading the heads and specimens at room temperature prior to insertion into the test unit.

Material Microstructure

The four wrought alloys were given the heat treatment mentioned in Table 1. Typical photomicrographs of alloy A-286, IN 800, N-155, and 19-9DL are shown in Fig. 5. The large grain sizes and twin boundaries may be seen in three alloys while the

significant carbide in the matrix of 19-9DI reflected its high carbon level (0.31%) and low annealing temperature (1790°F).

The as-cast microstructures of three alloys--namely, XF-818, SAF-11, and Stellite 6B--were more or less pore free as shown in Fig. 6. On the other hand, alloy CRM-6D had significant porosity, as may be seen in Figs. 7 and 8.

Material microstructures remained virtually unaffected due to permeation exposure at these temperatures up to 815°C (1500°F) which was considerably below the annealing temperatures of the wrought alloys. Microstructures of IN 800, N-155, XF-818, and SAF-11 exposed samples shown in Fig. 9 reveal observable difference between them and the received material microstructures. It is to be noted, however that in localized areas, SAF-11 can have significant porosity very close to the surface.

Test Equipment

Permeability measurements were made in a special test facility designed and fabricated by IITRI prior to initiation of the testing program. This facility was designed for operation at 20.7 MPa and temperatures to 1200°C. A schematic diagram of the facility is shown in Fig. 10. The system consists of a balanced pressure design in which the hydrogen pressure in the internal unit was balanced by nitrogen in the annulus between the permeability unit and the pressure vessel. An engineering drawing of the pressure vessel internals is shown in Fig. 11.

Hydrogen was supplied to the test unit from 41.4 MPa hydrogen tanks regulated to 22.8 MPa and then to 20.7 MPa. Hydrogen was then transported to the inlet side of the specimen through the fill tubing. A chromel-alumel thermocouple was maintained in contact with the test specimen during testing, but temperature control was maintained by a second thermocouple located in contact with the Nichrome furnace elements. Nitrogen in the jacketing volume balancing the hydrogen pressure in the test unit was metered in a similar manner to the hydrogen. A vacuum pump provided a means of evacuating both the inlet and exit side of the test specimen.

On the exit side of the test sample, hydrogen permeating through the specimen was transmitted through the exit tubing to the pressure measurement chamber. The volume of the exit tubing was very small compared to the test chamber. Pressure in the measurement chamber was measured by a thermistor gauge, model GT-340A, attached to a chart recorder.

Experimental Procedure

The specimen and upper and lower heads were assembled at room temperature outside the permeability test facility and subjected to a force of 900 N (4000 lbf) in a hydraulic press. This assembly was maintained under pressure with a clamping device during incorporation into the test unit. Subsequently, the clamping pressure was maintained by the adjustable spring loading assembly at the top of the test vessel. The output chamber was then attached, and the inlet and exit sides checked for an acceptable leak rate of 2.8×10^{-5} ml/s. If the seals were adequate, the assembly was heated to 650°C and held at temperature overnight prior to permeability measurements.

At the beginning of a permeability test, the output side seal leak rate was checked first by monitoring the leak rate of the measurement chamber. If the leak rate was acceptable, the jacket was exposed to 20.7 MPa nitrogen pressure with a vacuum maintained on the inlet side of the test sample for 3600 seconds. Following this process, the outlet chamber was isolated and the nitrogen leak rate into the measurement chamber was monitored for at least 1800 seconds. This test provided the leak rate correction for permeability measurements. After the leak rate measurement, the permeability measurement chamber was evacuated to 1.5 Pa (11 millitorr) and high purity (less than 5 ppm O_2) hydrogen was introduced to the inlet side of the specimen to begin the permeability test. The pressure rise measurement chamber was then monitored by the thermistor gauge for periods up to 1.8×10^4 seconds.

For multiple temperature tests, both sides of the test sample were evacuated following the permeability test. The temperature was then reset to the temperature selected for the subsequent day's test. The specimen was again held overnight at the selected test temperature prior to the second test. In most cases, multiple temperature tests were conducted without cooling to room temperature. At least duplicate permeability tests were conducted for each alloy at four temperatures over the range 650°-815°C. It was common practice to conduct one test at each temperature in an increasing temperature sequence and the second test on a decreasing temperature schedule.

Prior to permeability tests, the output (measurement) vessel was calibrated by injecting known volumes of hydrogen into the chamber. This test was conducted several times with several volumes of both hydrogen and nitrogen. The system calibration curves for nitrogen and hydrogen are reproduced in Figs. 12 and 13, respectively. These calibration curves convert millivolt output of the thermistor gauge directly into volume of hydrogen and nitrogen at the chamber temperature, which can then be converted to H_2 and N_2 volumes at standard pressure and temperature.

At the conclusion of each permeation test, the nitrogen leak rate was calculated by using the recorder output and the nitrogen calibration curve (Fig. 12). This leak rate was generally found to be linearly time dependent, and was measured for at least 1800 s prior to commencing each permeation test. Since the hydrogen permeation thermistor gauge trace consists of millivolt output due both to the nitrogen "leak" and to the hydrogen permeating through the sample, the nitrogen trace was subtracted from the hydrogen permeation trace shown in Fig. 14. This difference provided a third plot of millivolt output versus time due to hydrogen permeation alone, converted to a plot of ml of hydrogen (STP) versus time using the calibration curve shown in Fig. 13. A typical final plot of hydrogen permeation versus time for test B2 (IN 800) is shown in Fig. 15.

Calculation of Permeability (Ø)

Using plots such as that shown in Fig. 15, and the permeability calculation methods described earlier, the following represents a sample calculation of permeability, diffusivity, and solubility values. Both permeability (Ø) and diffusivity (D) are measurable quantities determined from plots such as that in Fig. 15, whereas solubility values were derived from the measured quantitites. During permeation tests, there was always a time interval from the time hydrogen gas was introduced to the inlet side specimen until it emerged at a constant rate from the exit side. The steady-state or linear portion of Fig. 15 is related to the permeation flux, j_t, according to the relationship:

$$\text{Slope of linear region, } \tan \alpha = j_t \tag{18}$$

which for Fig. 15 has the units $cm^3\ s^{-1}$. Accordingly, for IN 800 (sample B2) tested at 815°C

$$j_{t(815°C)} = 1.17 \times 10^{-4}\ cm^3\ s^{-1} \tag{19}$$

The permeation rate (j_t) through the sample is related to the permeability (Ø) according to the equation:

$$j_t = \emptyset \frac{A}{\Delta x} (p_i^{\frac{1}{2}} - p_o^{\frac{1}{2}}) \tag{1}$$

where j_t = permeation flux, $cm^3\ s^{-1}$

Ø = permeability, $cm^3\ cm^{-1}\ s^{-1}\ MPa^{-\frac{1}{2}}$

A = specimen permeation area, cm^2

Δx = specimen thickness, cm

p_i = input pressure, MPa

p_o = output pressure, MPa

For specimen B2 at 815°C,

$$\Delta x = 0.576 \text{ cm}$$

$$A = 0.785 \text{ cm}^2$$

$$p_i = 20.7 \text{ MPa}$$

$$p_o = 1.5 \text{ Pa}$$

$$j_t = 1.17 \times 10^{-4} = \phi \cdot \frac{(0.785)}{(0.576)} \quad (4.55)$$

Therefore, $\phi = 1.9 \times 10^{-5} \text{ cm}^3 \text{ cm}^{-1} \text{ s}^{-1} \text{ MPa}^{-\frac{1}{2}}$

Since testing was done at approximately 25°C (i.e., standard temperature), then

$$\phi = 1.9 \times 10^{-5} \text{ cm}^3 \text{ (STP) cm}^{-1} \text{ s}^{-1} \text{ MPa}^{-\frac{1}{2}}$$

Calculation of Diffusivity Term (D)

The "lag time," θ_L--the intercept which the steady-state portion of the curves makes with the time axis (Fig. 15)--is related to the diffusion term (D) for this system, according to the equation:

$$\theta_L = \frac{(\Delta x)^2}{6D} \quad (17)$$

For IN 800 (specimen B2) at 815°C (from Fig. 15):

$$\theta_L = 1875 \text{ s}$$

Therefore, $D = \frac{(0.576)^2}{6 \times 1875}$

$$= 2.95 \times 10^{-5} \text{ cm}^2 \text{ s}^{-1}$$

Derivation of Solubility Term (K)

It has been mentioned earlier that using the ideal gas law and Sievert's relationship, and several implied assumptions, it is possible to derive some information regarding the solubility term at these high temperatures. The relationship in Equation 6,

$$\phi = DK$$

can be used for the above data for IN 800. Using $\phi = 1.9 \times 10^{-5}$ cm^3 (STP) cm^{-1} s^{-1} $\text{MPa}^{-\frac{1}{2}}$ and $D = 2.95 \times 10^{-5}$ cm^2 s^{-1}, and Equation 6,

$$K = \frac{1.9 \times 10^{-5}}{2.95 \times 10^{-5}}$$

$$= 0.64 \text{ cm}^3 \text{ cm}^{-3} \text{ MPa}^{-\frac{1}{2}}$$

It is to be realized, however, that the permeation, diffusivity, and solubility of H_2 in metals and alloys consist of many interrelated steps and processes and the use of permeability and diffusivity parameters alone to obtain solubility may not give a true measure of the parameter without additional measurements and corrections.

EXPERIMENTAL RESULTS

Uncoated Metals

Table 3 summarizes the permeability, diffusivity, and solubility data for all uncoated alloy specimens. Data in Table 3 include specimen thickness and test sequence, in addition to the experimentally determined hydrogen data. In some cases, a sample was retested after regrinding both the input and exit surfaces. These samples are identified in the table. All data generated for uncoated metals are included in Table 3. However, those data considered questionable have been eliminated from the least-squares analysis of the data plotted in this report. Data for N-155 at 6.9 MPa and 13.8 MPa at 815°C are included in Table 3. In the case of SAF-11, only one sample was suitable for testing; the duplicate tests were conducted on the same specimen after remachining.

In the early tests, i.e., for IN 800 and A-286, both tests were conducted in an increasing temperature sequence. For the remaining alloys, both heating and cooling sequences were employed. For alloys tested under both sequences, no significant influence of test sequence was determinable in the data. Some problems were experienced with the cast alloy specimens. It was not clear that cast alloys were completely free of casting cracks in their internal structures. Further, some shrinkage porosity may have existed in the cast alloy test samples of CRM-6D, SAF-11, and XF-818.

Individual permeability data for N-155 from Table 3 are plotted versus reciprocal of absolute temperature in Fig. 16. The least-squares fit of the various data is indicated in the plot. Similar plots for permeability coefficient for the remaining alloys in comparison to N-155 are presented in Fig. 17. In each case, a least-squares analysis of the data in Table 3 was employed to develop the temperature variation.

The plots in Fig. 17 indicate similar permeabilities for all alloys. However, the slopes of the best fit curve for LC 6B, and to a lesser extent that for SAF-11, were less than those of the remaining alloys.

A plot of the diffusion coefficient, D, of the eight alloys against 1/T is given in Fig. 18. The diffusivity of all alloys exhibited similar behavior versus temperature. Again, the cast alloy SAF-11 departed somewhat from the other alloys.

Solubility values derived and shown in Table 3 indicate that within the range of experimental variability they remained relatively constant with temperature. For endothermic H_2-metal systems, in the literature, there are examples of H_2 solubility increasing with temperature.(1)

Plots of permeability and diffusivity (Figs. 10 and 11) were employed to calculate apparent activation energies for these processes. Permeability and diffusivity coefficients were observed to vary with the absolute temperature following the Arrhenius relationship:

$$\phi = \phi_o \exp(-Q_\phi/RT)$$

and

$$D = D_o \exp(-Q_D/RT)$$

Values of the pre-exponential coefficients ϕ_o and D_o, and the activation energies Q_ϕ and Q_D, were calculated from Figs. 17 and 18. These data for uncoated superalloys are summarized in Table 4. Apparent activation energies for permeation were similar for most alloys, i.e., 12-20 kcal/mole. For alloy 6B (LC), a lower value of 8.1 kcal/mole was obtained. For diffusion, the apparent activation energies calculated from the data ranged from 10-20 kcal/mole. The similarity between activation energies for diffusion and permeation indicate that the assumption of diffusion control was essentially correct.

As shown in the earlier discussion, the activation energy of permeation is, in most cases of endothermic H_2 diffusion in metals, made up of some, or all, of several individual energies:(3)

a) energy of adsorption
b) energy of dissociation
c) energy of absorption
d) energy of diffusion
e) energy of desorption
f) energy of reassociation.

Calculated activation energies for solubility were considerably lower, with 5 kcal/mole being the largest value calculated. Depending on data scatter and relative activation energies of

permeation and diffusion, one may even obtain negative quantities. Unless independent and direct measurements of solubility are performed, the derived data will be reliable though it may be assumed that the activation energy for the solubility will be smaller than for both diffusion and permeation.

Coated Metals

Permeability data for the potential hydrogen barrier coatings on N-155 are summarized in Table 5. At present, it could not be ascertained if diffusion control existed for coated alloys, and diffusivity and solubility data were not calculated. The coatings, including Al_2O_3, Si_3N_4, glass, and a pack aluminide, were applied to the inlet side of the test sample. Problems were observed in adherence of the glass and Al_2O_3 coatings during permeability testing. After testing, the glass and Al_2O_3 coating had spalled from the surface; it was not known if the coating was adherent during testing. To avoid coating spalling problems, all coated alloys were tested only on an increasing temperature sequence beginning at 650°C. Typical appearance of an Al_2O_3-coated sample is shown in Fig. 19.

Permeability data summarized in Table 5 and plotted in Fig. 20 indicate that the pack aluminide (HWS 25000) coating provided the lowest hydrogen permeability rates. Permeability coefficients and apparent activation energies from Arrhenius analysis are listed in Table 6. The unusual permeation behavior shown by the glass-coated sample probably resulted from coating cracking and/or spalling of the coating. Based on the results shown in Table 5, the pack aluminide coating was selected for evaluation on the remaining iron-base alloys.

Table 7 is a summary of permeability data for pack aluminide coated (HWS 25000) A-286, 19-9DL, and IN 800. Least-squares best fit of the permeability data for coated alloys is plotted versus increasing absolute temperature in Fig. 21. Data for the uncoated alloys are included in Fig. 21 for comparison. The aluminide coating reduced hydrogen permeability by about a factor of five over the range 650°-815°C.

Apparent activation energies and pre-exponential coefficients for coated and uncoated alloys are compared in Table 8. Except for A-286, all activation energies for permeation were in the range of 10-25 kcal/mole.

SUMMARY OF RESULTS

Hydrogen permeability, diffusivity, and solubilities were measured for seven iron-base and one cobalt-base superalloys over the temperature range 650°-815°C. The effectiveness of four commercial coatings in reducing hydrogen permeability of four iron-base superalloys was assessed. The results of this study are summarized below:

1. Hydrogen permeability of all eight superalloys was similar in the range 650°-815°C and increased with increasing temperature. The cobalt-base alloy, low carbon 6B, indicated a lesser temperature dependence than iron-base alloys.

2. Diffusion and solubility coefficients were similar for all superalloys evaluated.

3. Apparent activation energies for permeability were in the range 15-25 kcal/mole for most alloys, similar to that obtained for diffusion. Activation energies for solubility were low, and most often below 5 kcal/mole.

4. An aluminide diffusion coating was most effective in reducing hydrogen permeability. A factor of five reduction in hydrogen permeability was determined over the range 650°-815°C. Alumina, silicon nitride, and glass coatings appeared to be less effective in reducing hydrogen permeability. However, cracking and spalling of these nondiffused coatings were observed on exposed specimens, thus diminishing their effectiveness.

5. Apparent activation energies for permeability of coated alloys were determined to be 10-25 kcal/mole, and possibly somewhat greater than those of the uncoated alloys.

REFERENCES

1. C. J. Smithells, Metals Reference Book, Vol. II, 4th ed., Plenum Press, New York, 1967, pp. 605-636.

2. Z. M. Turovtseva and L. L. Kernin, Analysis of Gases in Metals, Consultants Bureau, New York, 1959, pp. 5-28.

3. F. N. Rhines, "Gas-Metal Diffusion and Internal Oxidation," in Atom Movement, ASM, Cleveland, Ohio, 1951, pp. 174-191.

4. M. L. Hill and E. W. Johnson, "The Solubility of Hydrogen in Alpha Iron," Trans. AIME, Vol. 221, June 1961, pp. 622-629.

5. R. M. Barrer, Diffusion In and Through Solids, Macmillan, New York, 1941.

6. R. M. Barrer, Trans. Faraday Soc. (London), Vol. 35, 1939, p. 628.

Table 1

CHEMICAL COMPOSITION OF WROUGHT AND CAST SUPERALLOYS [a]

Element	SAF-11[b]	XF-818[b]	CRM-6D[b]	Stellite 6B	N-155	19-9DL	IN 800	A-286
C	0.64	0.23	1.11	0.41	0.11	0.31	0.08	0.05
Si	0.60	0.38	0.48	0.36	0.83	0.80	0.14	0.16
Mn	0.49	0.17	3.30	1.04	1.20	0.83	0.71	0.11
P	0.038	0.009	0.016	0.031	--	0.023	0.022	0.015
S	0.018	0.015	0.020	0.008	--	0.01	0.007	0.008
Fe	48.36	53.28	63.46	2.05	28.82	66.28	47.25	55.76
Ni	17.12	18.80	5.45	2.08	20.04	9.28	30.10	25.05
Cr	23.17	18.21	22.67	29.21	21.60	18.86	20.38	14.16
Mo	0.15	7.30	1.14	0.90	2.90	1.48	--	1.72
W	7.39	--	1.05	3.84	3.05	1.30	--	--
Cb + Ta	--	0.42	1.20	--	1.10	0.42	--	--
Ti	--	--	--	--	--	0.20	0.30	2.35
Co	--	--	--	59.80	20.50	--	--	--
Other	0.44B	1.1B	--	--	0.15N	0.13Cu	0.31Al	0.16Al 0.004B

[a] Composition in weight percent

[b] Cast alloys.

Heat treatment: Plates heated to the following temperatures in argon and air cooled:

N-155 - 1182°C (2160°F), Incoloy 800 - 1121°C (2050°F)

A-286 - 982°C (1800°F), 19-9 DL - 977°C (1790°F)

Table 2

DETAILS OF COATINGS APPLIED TO IRON-BASE SUPERALLOYS

Coating	Supplier	Coating Thickness, mm (mils)
Al_2O_3	Linde Division, Union Carbide	0.18 (7)[a]
Si_3N_4	CVC Products, Inc.	0.001 (0.04)[b]
S6100M[c]	Solar Division International Harvester	0.05 (2)[d]
HWS 25000[e]	Chromizing Corp.	0.06 (2.5)[e]

[a]Detonation gun coating.

[b]Chemical vapor deposition.

[c]Compositions not available.

[d]Slurry fuse coating.

[e]Pack diffusion aluminide.

Table 3

SUMMARY OF PERMEABILITY DATA FOR UNCOATED SUPERALLOYS

Material	Sample No.	Thickness, cm	Temp., °C	Test Sequence	Permeability (θ),[a] cm^3(STP) $cm^{-1}\ s^{-1}\ MPa^{-½}$	Diffusivity (D), $cm^2\ s^{-1}$	Solubility (K),[b] cm^3(STP) $cm^{-3}\ MPa^{-½}$
N-155	A1	0.616	815	4	1.9×10^{-5}	4.6×10^{-5}	0.41
	A2	0.598	650	4	3.9×10^{-6}	1.4×10^{-5}	0.28
			705	3	1.1×10^{-5}	2.1×10^{-5}	0.52
			760	2	2.3×10^{-5}	2.8×10^{-5}	0.82
			815	1	3.8×10^{-5}	4.8×10^{-5}	0.79
	A5	0.609	650	1	4.4×10^{-6}	7.3×10^{-6}	0.59
			705	2	4.6×10^{-6}	1.5×10^{-5}	0.31
			760	3	1.4×10^{-5}	1.9×10^{-5}	0.74
			815[c]	4	1.4×10^{-5}	2.3×10^{-5}	0.61
			815[d]	5	1.1×10^{-5}	1.8×10^{-5}	0.61
	A8	0.606	650	4	1.5×10^{-5}	1.6×10^{-5}	0.94
			705	3	1.4×10^{-5}	9.7×10^{-6}	1.44
			760	2	1.7×10^{-5}	1.6×10^{-5}	1.06
			815	1	2.4×10^{-5}	2.5×10^{-5}	0.96
			815	5	3.8×10^{-5}	2.9×10^{-5}	1.31
IN 800	B1	0.548	650	4	5.9×10^{-6}	7.1×10^{-6}	0.83
			705	3	1.0×10^{-5}	1.1×10^{-5}	0.91
			760	2	1.8×10^{-5}	2.2×10^{-5}	0.82
			815	1	2.8×10^{-5}	3.7×10^{-5}	0.76
	B2	0.576	650	1	6.1×10^{-6}	6.9×10^{-6}	0.88
			705	2	1.1×10^{-5}	1.2×10^{-5}	0.92
			760	3	1.2×10^{-5}	1.3×10^{-5}	0.92
			815	4	1.9×10^{-5}	3.0×10^{-5}	0.64
19-9DL	C1	0.544	650	4	2.8×10^{-6}	7.6×10^{-6}	0.37
			705	3	6.3×10^{-6}	8.8×10^{-6}	0.72
			760	2	1.4×10^{-5}	1.6×10^{-5}	0.88
			815	1	1.0×10^{-5}	3.4×10^{-5}	0.47
	C2	0.555	650	1	5.6×10^{-6}	6.4×10^{-6}	0.88
			705	2	7.0×10^{-6}	1.1×10^{-5}	0.64
			760	3	1.4×10^{-5}	1.3×10^{-5}	1.08
			815	4	2.0×10^{-5}	2.0×10^{-5}	1.00
A-286	D2	0.557	650	1	8.4×10^{-6}	9.8×10^{-6}	0.86
			705	2	1.5×10^{-5}	1.5×10^{-5}	1.00
			760	3	1.8×10^{-5}	2.2×10^{-5}	0.82
			815	4	2.3×10^{-5}	2.9×10^{-5}	0.79
	D4	0.610	650	1	9.1×10^{-6}	1.2×10^{-5}	0.76
			705	2	1.2×10^{-5}	1.7×10^{-5}	0.71
			760	3	1.8×10^{-5}	2.9×10^{-5}	0.62
			815	4	3.8×10^{-5}	4.5×10^{-5}	0.84
CRM 6D	J1	0.637	650	4	1.6×10^{-5}	3.8×10^{-5}	0.42
			705	3	2.7×10^{-5}	4.2×10^{-5}	0.64
			760	2	4.7×10^{-5}	7.0×10^{-5}	0.67
			815	1	5.9×10^{-5}	1.1×10^{-4}	0.54

Table 3 (cont.)

Material	Sample No.	Thickness, cm	Temp., °C	Test Sequence	Permeability (θ).[a] cm^3 (STP) cm^{-1} s^{-1} $MPa^{-\frac{1}{2}}$	Diffusivity (D), cm^2 s^{-1}	Solubility (K).[b] cm^3 (STP) cm^{-3} $MPa^{-\frac{1}{2}}$
	J2-1	0.653	650	1	8.8×10^{-6}	1.3×10^{-5}	0.68
			705	2	2.4×10^{-5}	8.5×10^{-6}	2.82
			760	3	4.1×10^{-5}	1.7×10^{-5}	2.41
			815	4	5.8×10^{-5}	2.3×10^{-5}	2.52
	J2-2[e]	0.587	650	4	8.1×10^{-6}	7.0×10^{-6}	1.16
			705	3	1.4×10^{-5}	9.6×10^{-6}	1.46
			760	1	1.3×10^{-5}	1.8×10^{-5}	0.72
			815	2	2.2×10^{-5}	2.8×10^{-5}	0.79
LC 6B	K1	0.615	705	2	3.8×10^{-5}	2.4×10^{-5}	1.58
			760	3	1.7×10^{-5}	2.8×10^{-5}	0.61
			815	4	1.7×10^{-5}	5.1×10^{-5}	0.33
	K2	0.612	650	4	6.3×10^{-6}	9.1×10^{-6}	0.69
			705	3	1.5×10^{-5}	8.7×10^{-6}	1.72
			760	2	1.7×10^{-5}	1.9×10^{-5}	0.89
			815	1	2.0×10^{-5}	4.1×10^{-5}	0.49
	K3-1	0.615	650	4	2.7×10^{-5}	4.0×10^{-6}	6.75
			705	3	2.8×10^{-5}	7.5×10^{-6}	3.73
			760	2	6.9×10^{-5}	1.1×10^{-5}	6.27
			815	1	6.1×10^{-5}	1.8×10^{-5}	3.39
	K3-2[e]	0.585	650	1	1.8×10^{-5}	6.0×10^{-6}	3.00
			705	2	1.9×10^{-5}	9.6×10^{-6}	1.98
			760	3	2.6×10^{-5}	1.5×10^{-5}	1.73
			815	4	3.8×10^{-5}	2.6×10^{-5}	1.46
SAF-11	P2-1	0.624	650	4	2.4×10^{-5}	4.4×10^{-6}	5.45
			705	3	3.1×10^{-5}	8.5×10^{-6}	3.65
			760	2	5.0×10^{-5}	1.2×10^{-5}	4.17
			815	1	4.1×10^{-5}	2.2×10^{-5}	1.86
	P2-2[e]	0.608	650	4	6.3×10^{-6}	1.2×10^{-5}	0.53
			705	3	1.3×10^{-5}	1.1×10^{-5}	1.18
			760	2	1.8×10^{-5}	2.1×10^{-5}	0.86
			815	1	2.4×10^{-5}	3.1×10^{-5}	0.77
XF-818	Q1	0.637	650	4	1.4×10^{-5}	1.0×10^{-5}	1.40
			705	3	2.4×10^{-5}	1.6×10^{-5}	1.50
			760	2	3.0×10^{-5}	2.3×10^{-5}	1.30
			815	1	2.3×10^{-5}	4.0×10^{-5}	0.58
	Q4	0.633	650	2	8.8×10^{-6}	1.3×10^{-5}	0.68
			705	3	1.9×10^{-5}	1.2×10^{-5}	1.58
			760	4	2.6×10^{-5}	2.0×10^{-5}	1.30
			815	1	3.1×10^{-5}	3.2×10^{-5}	0.97
			815	5	4.7×10^{-5}	2.6×10^{-5}	1.81

[a]To convert to units of cm^3(STP) cm^{-1} s^{-1} $atm^{-\frac{1}{2}}$, multiply by 0.32.

[b]To convert to units of cm^3(STP) cm^{-3} $atm^{-\frac{1}{2}}$, multiply by 0.32.

[c]13.8 MPa hydrogen pressure.

[d]6.9 MPa hydrogen pressure.

[e]Second series of tests after remachining surfaces.

Table 4

SUMMARY OF ACTIVATION ENERGY AND PRE-EXPONENTIAL COEFFICIENTS FOR UNCOATED ALLOYS

	Permeability		Diffusivity		Solubility
Material	ϕ_o, cm^3 (STP) $cm^{-1}\ s^{-1}\ MPa^{-\frac{1}{2}}$	Q_ϕ, kcal/mole	D_o, $cm^2\ s^{-1}$	Q_D, kcal/mole	K_o, cm^3 (STP) $cm^3\ MPa^{-\frac{1}{2}}$
N-155	1.7×10^{-1}	18.8	1.6×10^{-2}	13.5	1.0×10^{1}
IN 80	4.1×10^{-2}	16.2	1.3×10^{-1}	18.1	3.2×10^{-1}
19-9DL	1.4×10^{-1}	19.2	3.2×10^{-2}	15.6	4.2×10^{0}
A-286	2.1×10^{-2}	14.3	3.3×10^{-2}	14.7	6.0×10^{-1}
CRM-6D	9.2×10^{-2}	16.5	1.5×10^{-2}	13.0	6.1×10^{0}
LC 6B	1.4×10^{-3}	8.1	2.6×10^{-1}	19.6	5.2×10^{-3}
SAF-11	8.3×10^{-3}	11.8	3.3×10^{-2}	15.6	2.4×10^{-1}
XF-818	1.1×10^{-2}	12.4	1.3×10^{-2}	13.0	8.5×10^{-1}

Table 5

SUMMARY OF PERMEABILITY DATA FOR COATED N-155[a]

Coating	Sample No.	Thickness cm	Temp., °C	Test Sequence	Permeability ϕ, cm^3 (STP) cm^{-1} s^{-1} $MPa^{-\frac{1}{2}}$
Al_2O_3	A112	0.605	650	4	6.8×10^{-6}
			705	3	1.1×10^{-5}
			760	2	1.2×10^{-5}
			815	1	1.4×10^{-5}
	A117	0.610	815	1	1.1×10^{-5}
	A115	0.606	650	1	2.0×10^{-5}
			705	2	6.2×10^{-5}
			760	3	9.2×10^{-5}
	A213	0.617	705	2	1.8×10^{-5}
			760	3	2.7×10^{-5}
			815	4	2.7×10^{-5}
Si_3N_4	A109	0.610	650	1	7.2×10^{-6}
			705	2	1.0×10^{-5}
			760	3	1.6×10^{-5}
			815	4	2.6×10^{-5}
	A110	0.611	650	1	1.2×10^{-5}
			705	2	2.3×10^{-5}
			760	3	2.9×10^{-5}
			815	4	4.4×10^{-5}
S6100M	A100	0.602	650	1	3.8×10^{-5}
			705	2	2.5×10^{-5}
			760	3	1.3×10^{-5}
			815	4	7.3×10^{-5}
HWS 25000	A107	0.612	760	2	5.0×10^{-7}
			815	1	4.9×10^{-7}
	A106	0.610	650	6	5.8×10^{-7}
			705	5	2.1×10^{-6}
			760	3	1.1×10^{-5}
			815	4	7.3×10^{-6}
	A104	0.609	650	4	2.6×10^{-6}
			705	3	8.8×10^{-6}
			760	2	1.1×10^{-5}
			815	1	7.2×10^{-6}

[a]Coating on inlet side only.

Table 6

SUMMARY OF ACTIVATION ENERGY AND PRE-EXPONENTIAL COEFFICIENTS FOR COATED N-155

		Permeability	
Coating	Type	ϕ_o, $cm^3(STP)\ cm^{-1}\ s^{-1}\ MPa^{-\frac{1}{2}}$	Q_ϕ, kcal/mole
Al_2O_3	Detonation gun coated	1.3×10^{-4}	3.71
Si_3N_4	Vapor deposited	3.9×10^{-2}	15.3
S6100M	Cracked glass	6.7×10^{-10}	a
HWS 25000	Pack aluminide	2.3×10^{-4}	8.7
Uncoated	--	1.7×10^{-1}	18.8

[a]Cracked glass coating, data unreliable.

Table 7

SUMMARY OF PERMEABILITY DATA FOR PACK ALUMINIDE COATED 19-9DL, A-286, AND IN 800[a]

Material	Sample No.	Thickness cm	Temp., °C	Test Sequence	Permeability ϕ, cm^3 (STP) $cm^{-1}\ s^{-1}\ MPa^{-\frac{1}{2}}$
IN 800	B101	0.617	650	1	5.0×10^{-7}
			705	2	9.1×10^{-6}
			760	3	5.0×10^{-6}
			815	4	4.4×10^{-6}
IN 800	B203	0.630	650	4	8.1×10^{-7}
			705	3	1.4×10^{-6}
			760	2	5.0×10^{-6}
			815	1	8.8×10^{-6}
19-9DL	C100	0.587	650	4	1.3×10^{-6}
			705	3	2.2×10^{-6}
			760	2	3.4×10^{-6}
			815	1	5.6×10^{-6}
19-9DL	C102	0.587	650	4	1.5×10^{-6}
			705	3	2.0×10^{-6}
			760	2	5.0×10^{-6}
			815	1	6.6×10^{-6}
A-286	D100	0.531	650	1	3.8×10^{-6}
			760	3	2.5×10^{-6}
			815	4	2.1×10^{-6}
A-286	D104	0.523	650	4	2.5×10^{-6}
			705	3	5.0×10^{-6}
			760	2	5.3×10^{-6}
			815	1	7.8×10^{-6}
A-286	D202	0.523	650	4	1.6×10^{-6}
			705	3	2.9×10^{-7}
			760	2	2.0×10^{-6}
			815	1	2.3×10^{-6}

[a]Coated on inlet side with HWS 25000.

Table 6

COMPARISON OF ACTIVATION ENERGY AND PRE-EXPONENTIAL COEFFICIENTS FOR PACK ALUMINIDE COATED AND UNCOATED N-155 IN 800, 19-9DL, and A-286

Material	Permeability ϕ_o, cm^3 (STP) $cm^{-1}\ s^{-1}\ MPa^{-\frac{1}{2}}$	Permeability Q_ϕ, kcal/mole
	Uncoated	
N-155	1.7×10^{-1}	18.8
IN 800	4.1×10^{-2}	16.2
19-9DL	1.4×10^{-1}	19.2
A-286	2.1×10^{-2}	14.3
	HWS 25000 Coated	
N-155	2.3×10^{-4}	8.7
IN 800	1.8×10^{0}	26.6
19-9DL	3.1×10^{-2}	18.4
A-286	2.4×10^{-6}	a

[a]Negligible effect of temperature was noted.

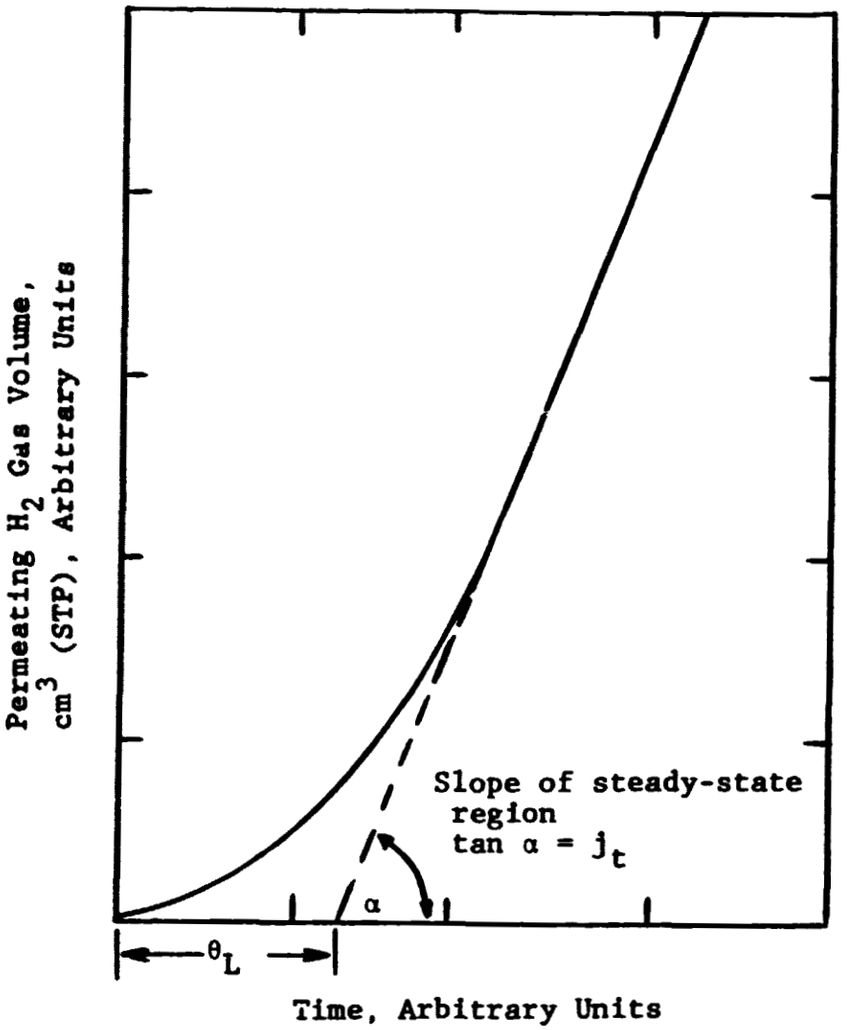

Figure 1

Schematic Representation of Hydrogen Gas Permeating a Solid Material Versus Time

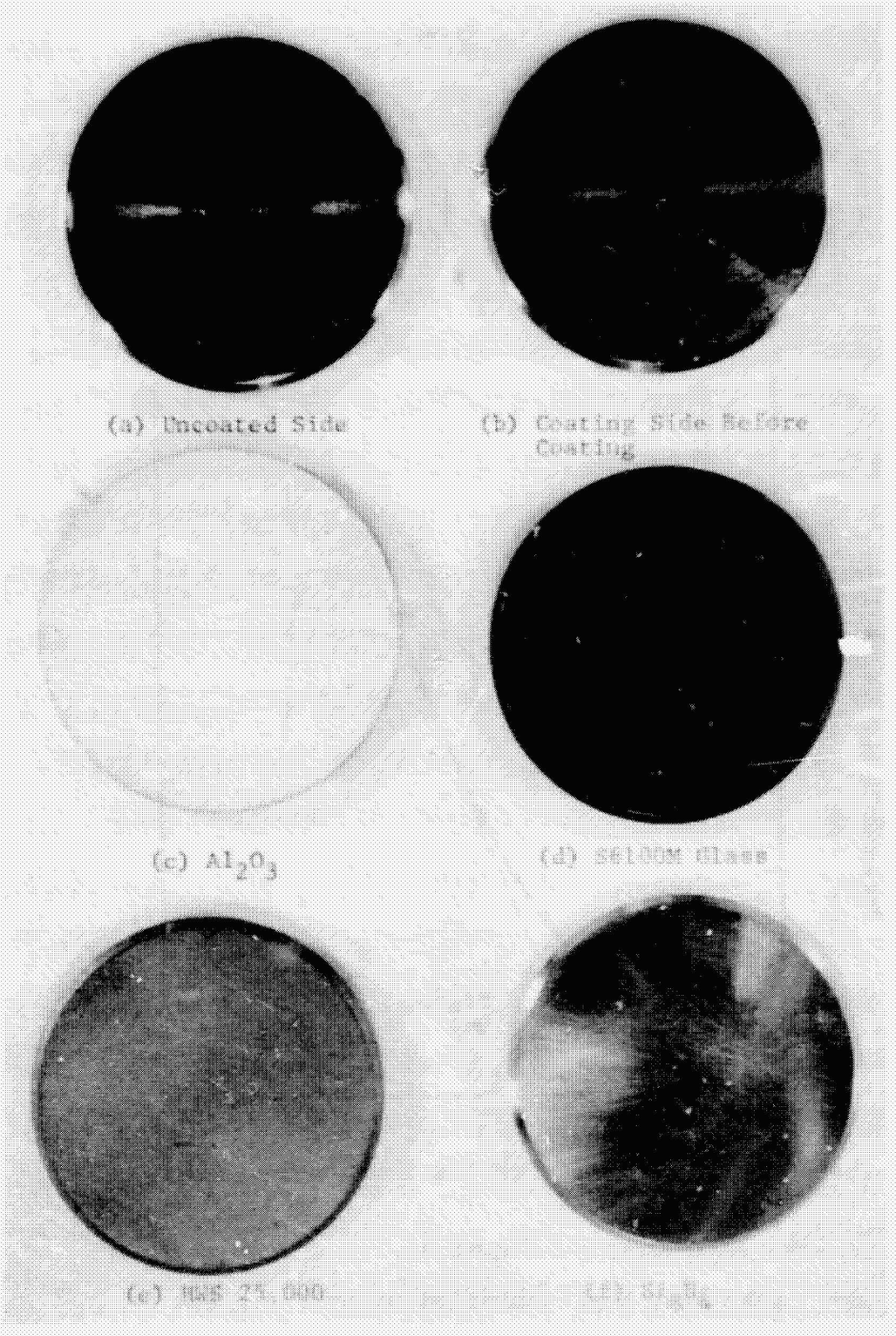

Figure 2

Appearance of Typical Uncoated and Coated Specimens

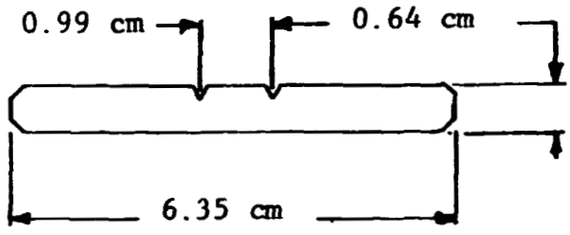

(a)

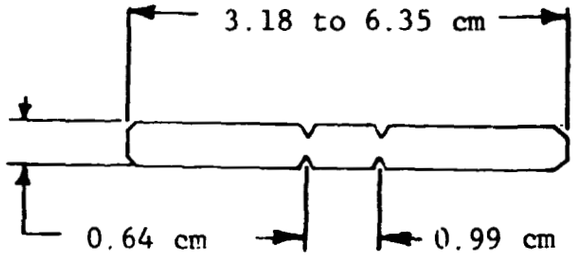

(b)

Figure 3

Specimen Design for (a) Coated and (b) Uncoated Specimens

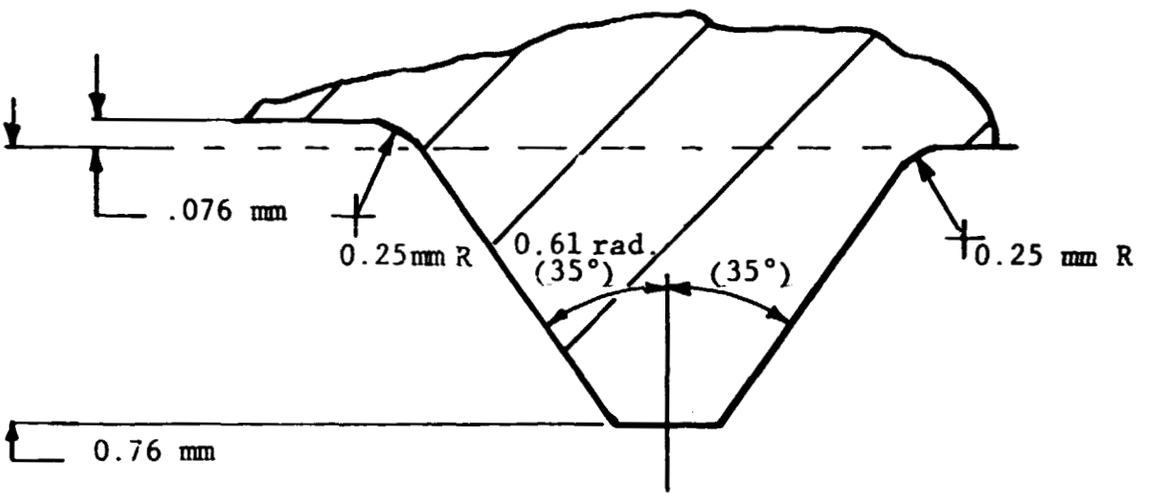

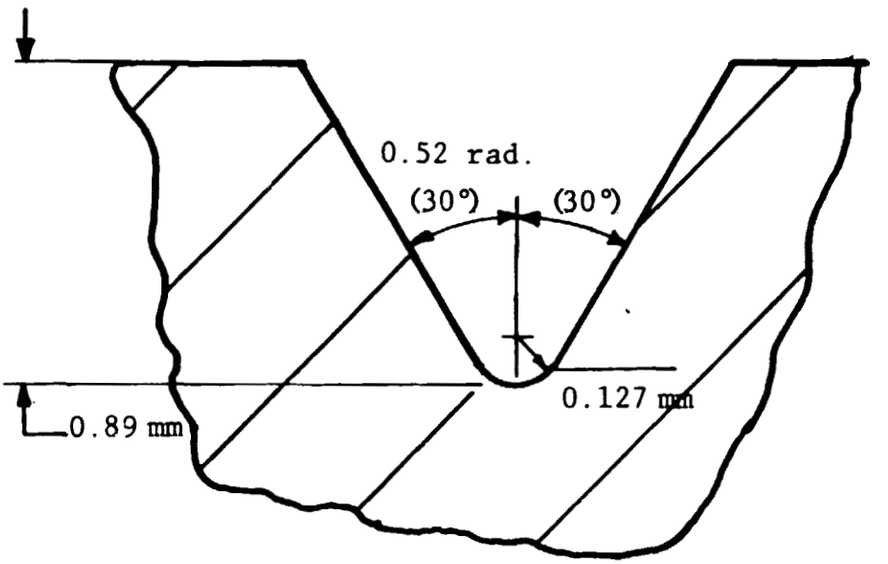

Figure 4

Details of High-Pressure Specimen Seal Design

Neg. No. 48139 200X

(a)

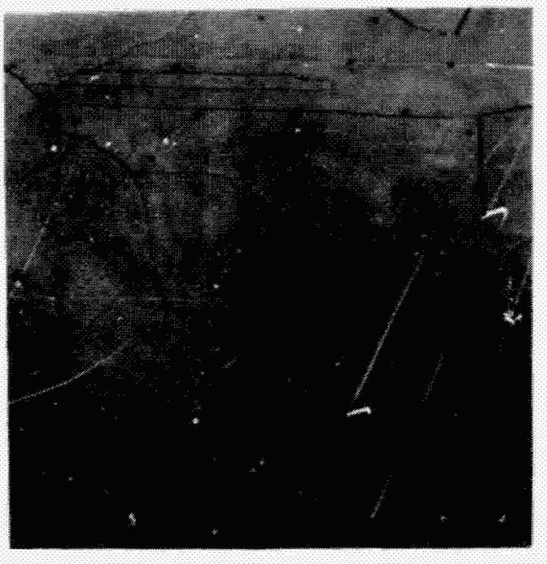

Neg. No. 48082 200X

(b)

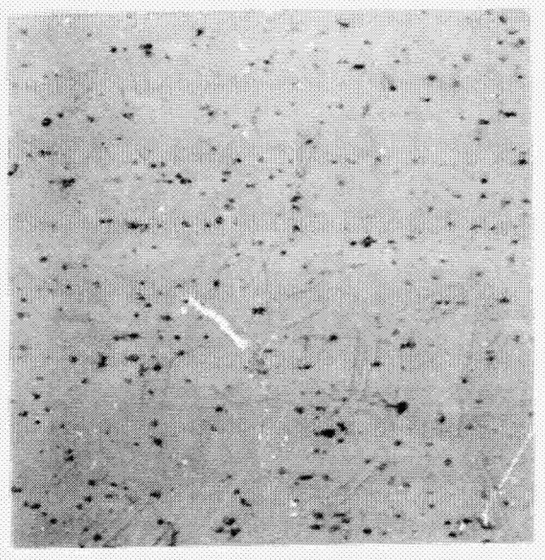

Neg. No. 48041 100X

(c)

Neg. No. 48134 200X

(d)

Figure 5

Typical Photomicrographs of Annealed Wrought Alloys.
(a) A-286, (b) IN 800, (c) N-155, and (d) 19-9DL.

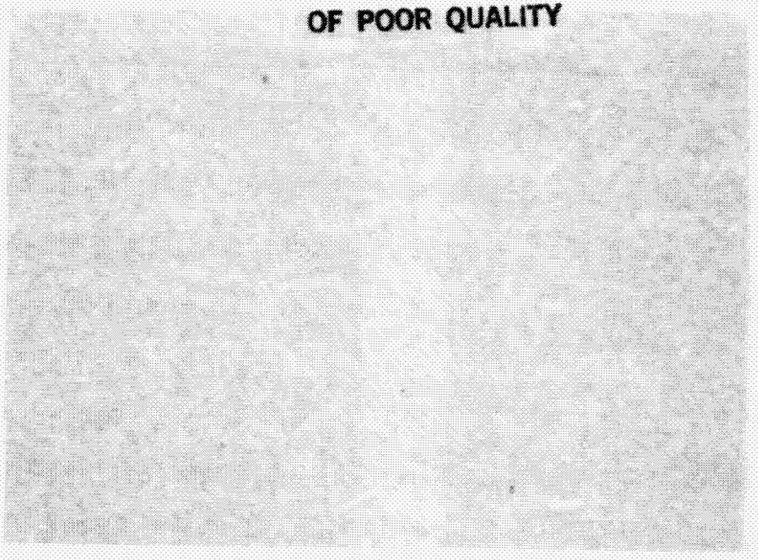

Neg. No. 52030 100X

(a)

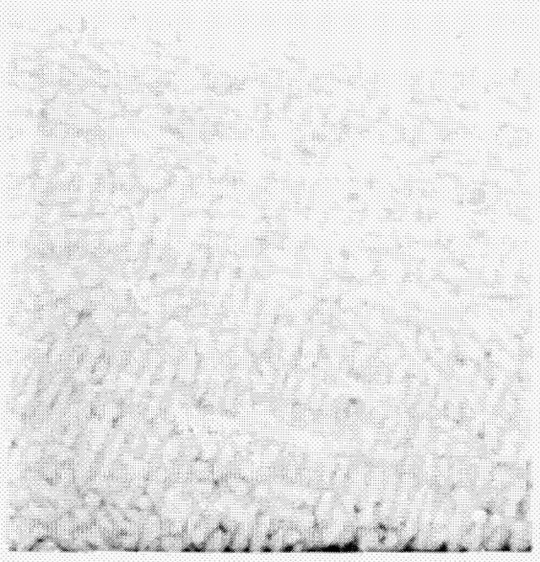

Neg. No. 52031 100X

(b)

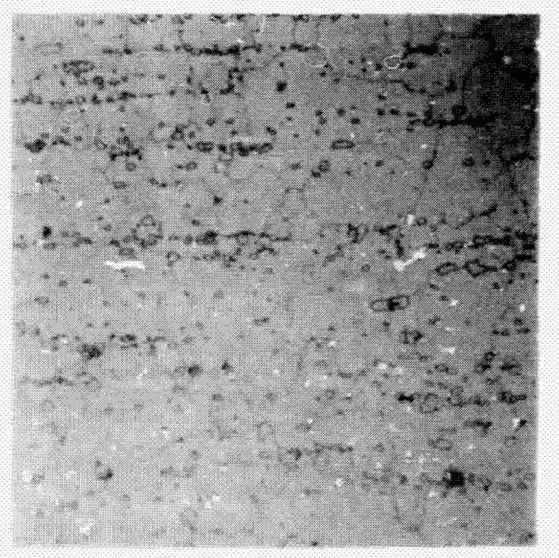

Neg. No. 50754 100X

(c)

Figure 6

Photomicrographs of Cast Alloys Showing Essentially Pore-Free Structures. (a) XF-818, (b) SAF-11, and (c) Stellite 6B.

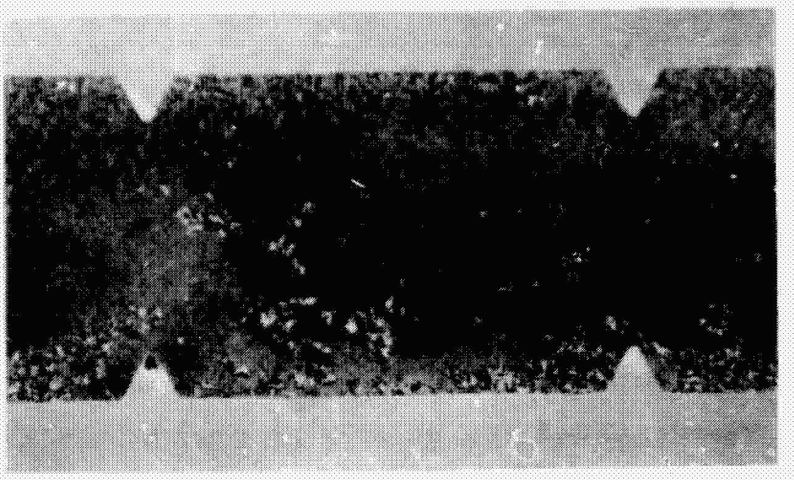

Neg. No. 50755 7X

(a) Distribution of casting defects over the permeation area

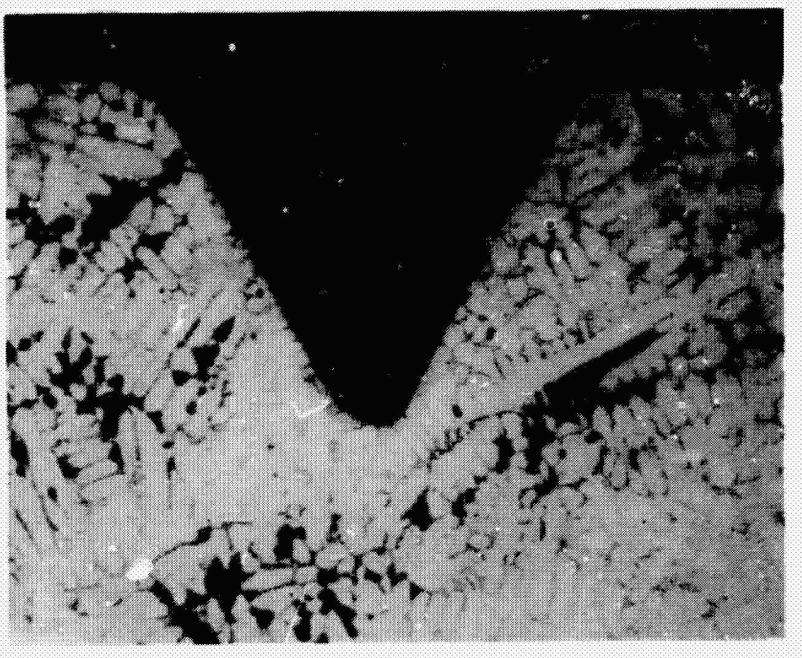

Neg. No. 50748 50X

(b) Significant porosity near a seal groove

Figure 7

Macrophotos of CRM-6D after Testing

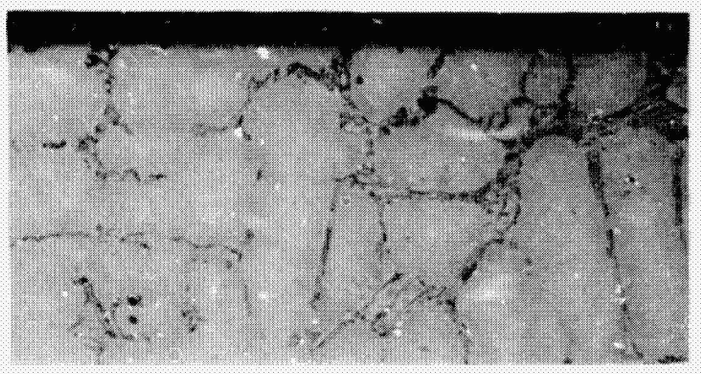

Neg. No. 50751 200X

(a) High-pressure H_2 side of CRM-6D after testing

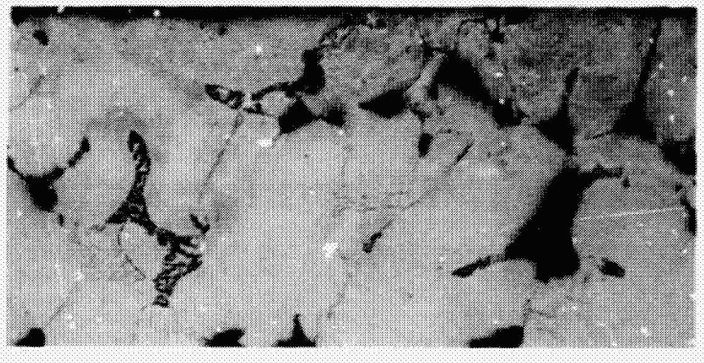

Neg. No. 50749 200X

(b) Low-pressure H_2 side of CRM-6D after testing

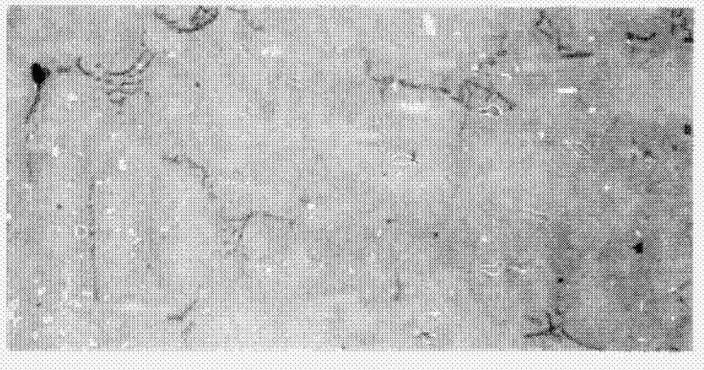

Neg. No. 57050 200X

(c) Center of CRM-6D specimen after testing

Figure 8

Microstructure of CRM-6D after Testing

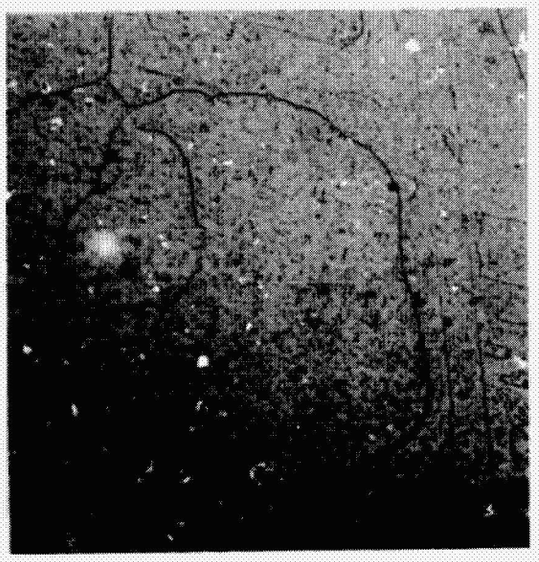

Neg. No. 50194 200X

(a)

Neg. No. 52421 200X

(b)

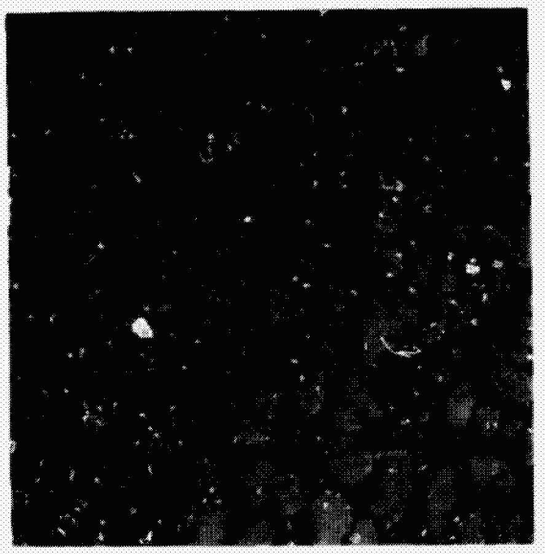

Neg. No. 52028 200X

(c)

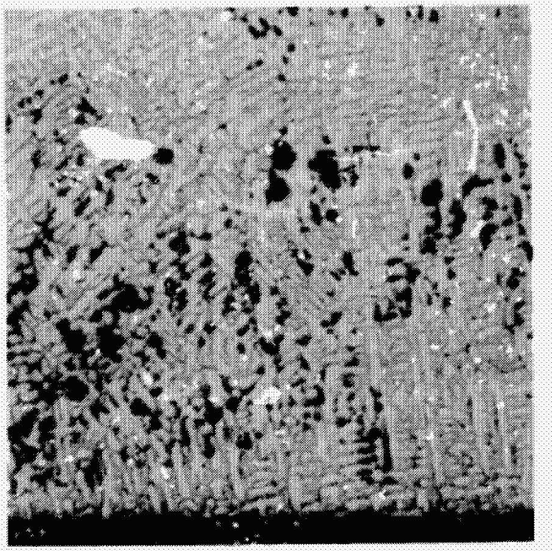

Neg. No. 52025 50X

(d)

Figure 9

Microstructures of Specimens after Hydrogen Permeation. (a) N-155, sample A-106; (b) IN 800, sample B400; (c) XF-818, sample Q4; and (d) SAF-11, sample P2-1.

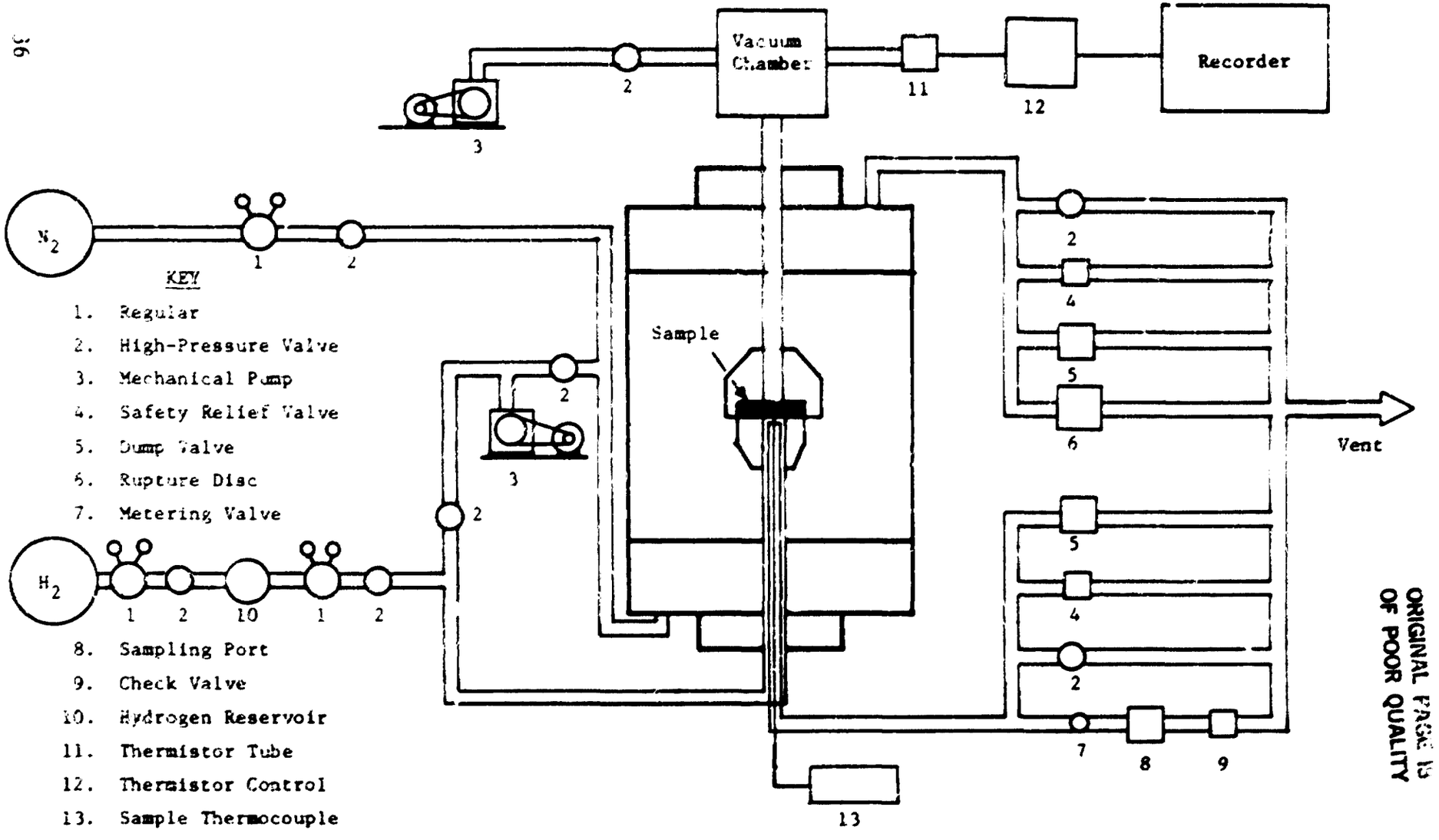

Figure 10

Schematic Diagram of the High Pressure-High Temperature Permeation System

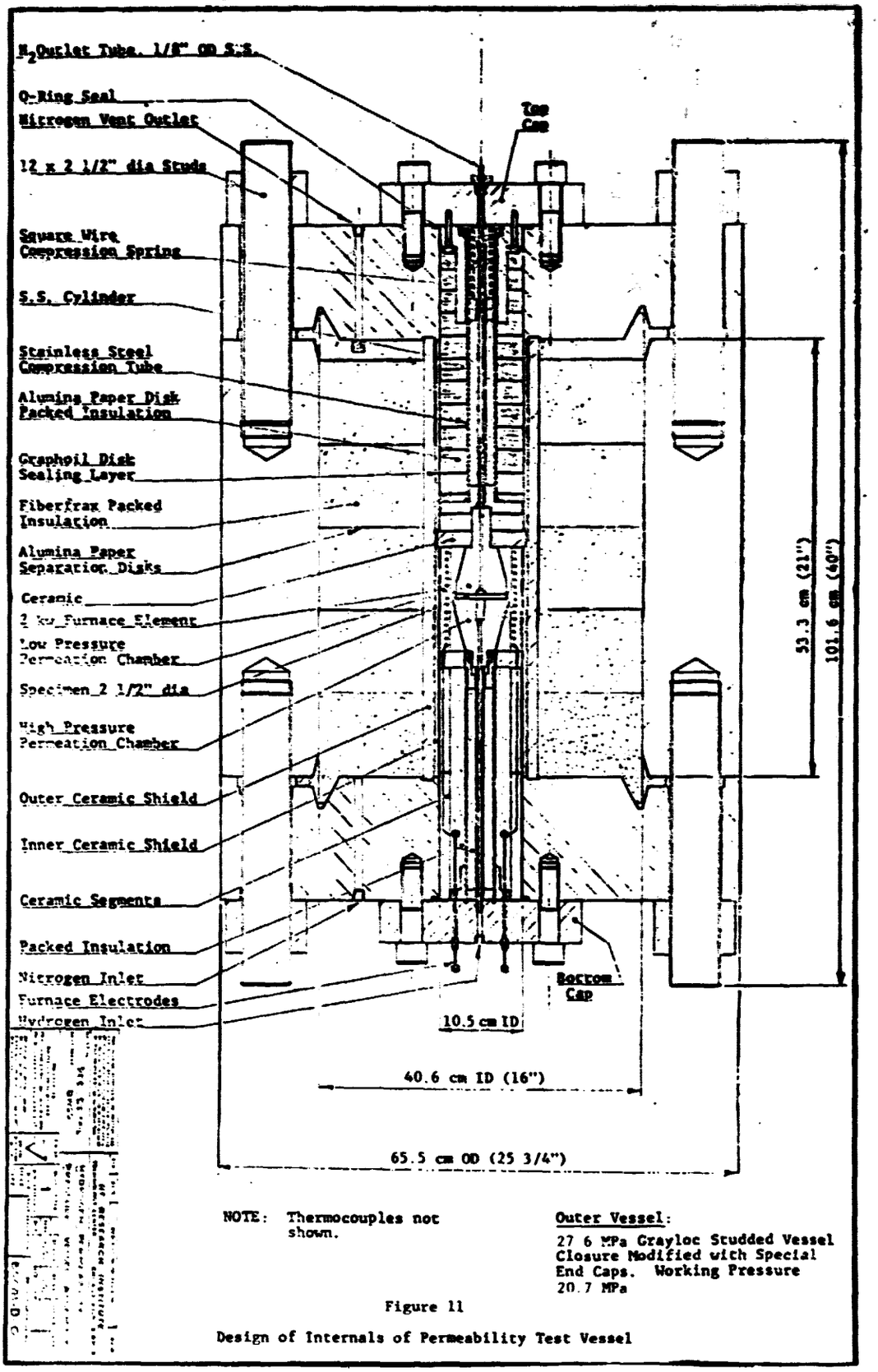

NOTE: Thermocouples not shown.

Outer Vessel:

27 6 MPa Grayloc Studded Vessel Closure Modified with Special End Caps. Working Pressure 20.7 MPa

Figure 11

Design of Internals of Permeability Test Vessel

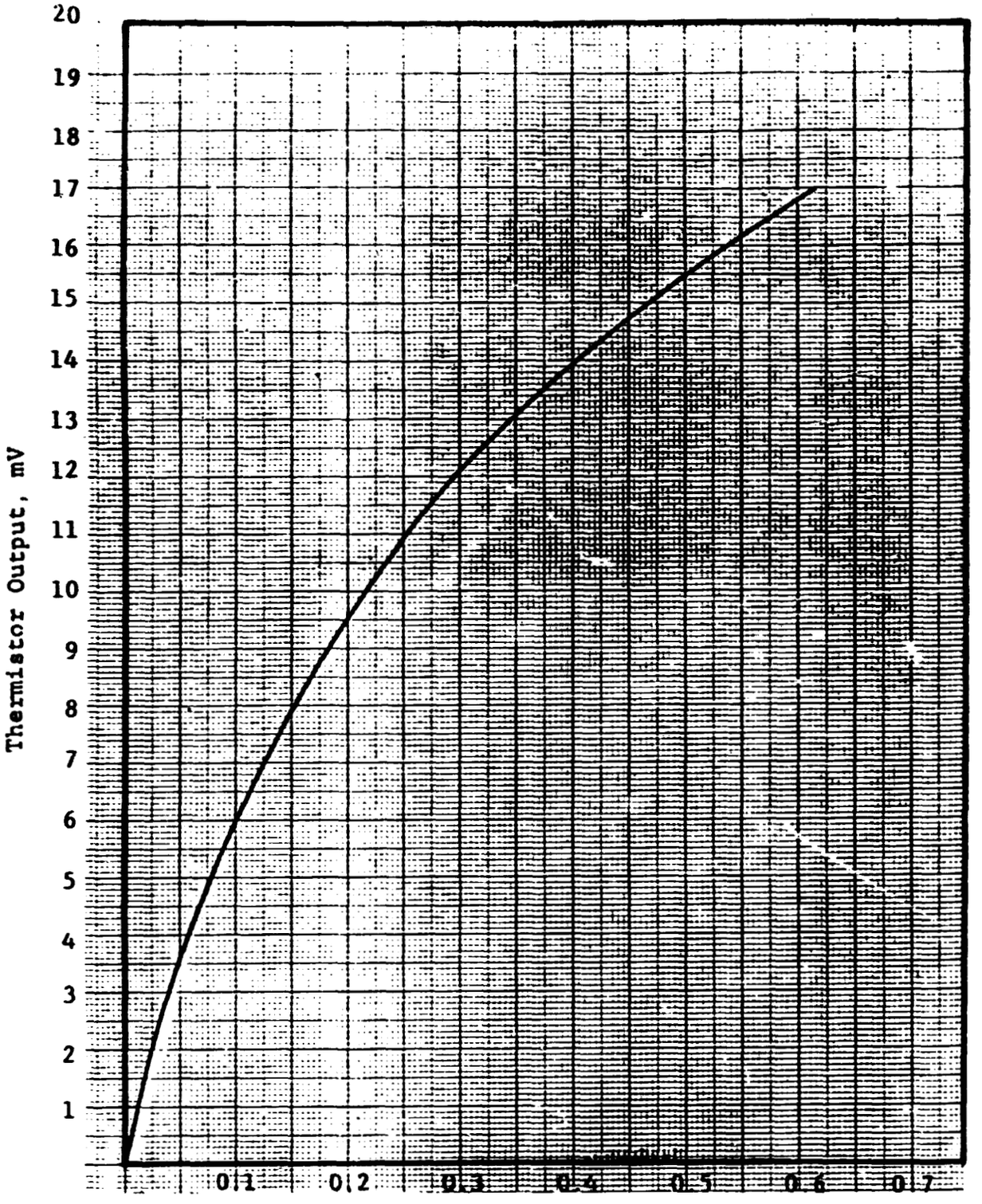

Figure 12

Calibration Curve for Detection Vessel/Thermistor Gauge System for Converting Thermistor Output (millivolts) to Nitrogen Volume (ml)

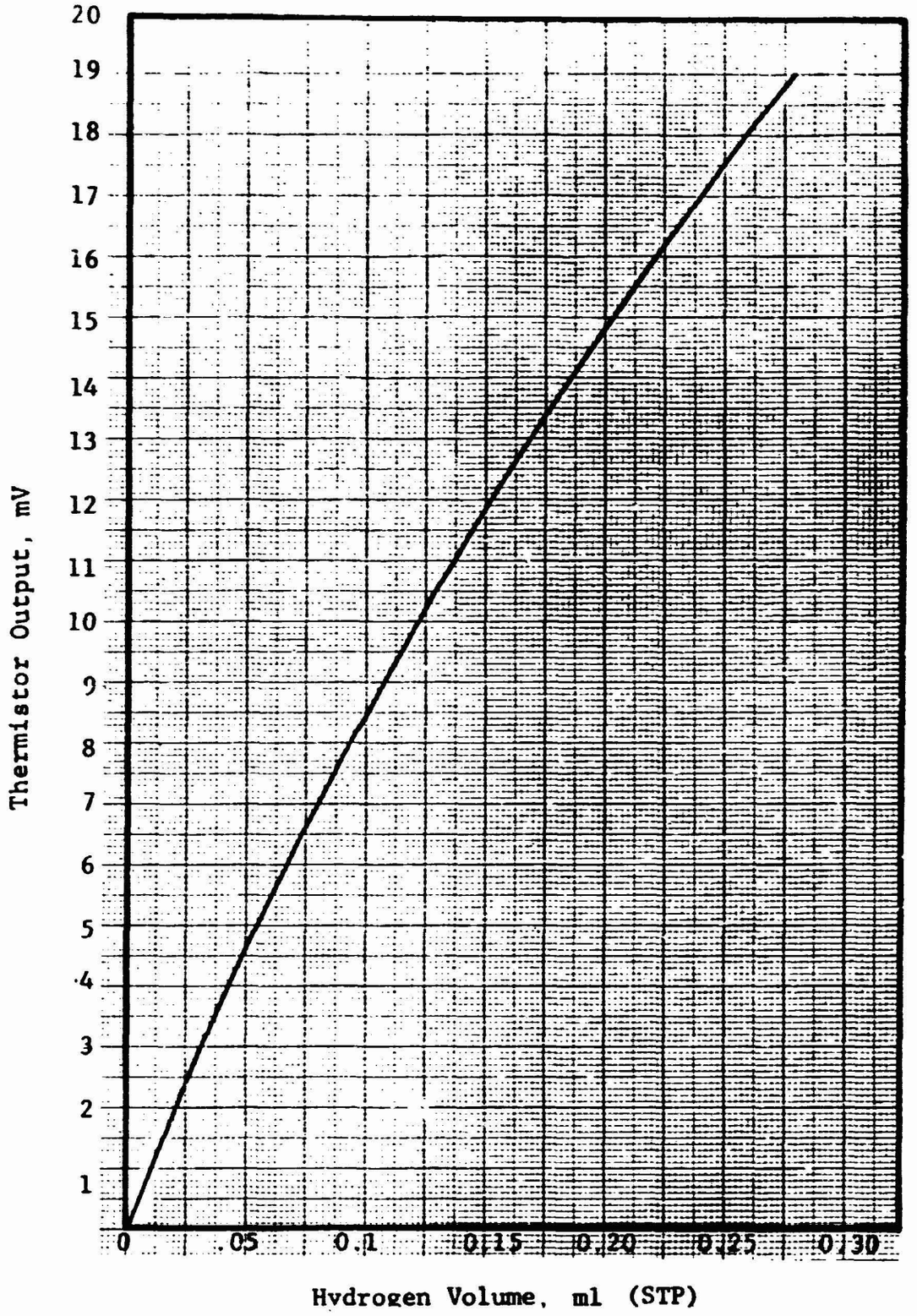

Figure 13

Calibration Curve for Detection Vessel/Thermistor Gauge System for Converting Thermistor Output (millivolts) to Hydrogen Volume (ml)

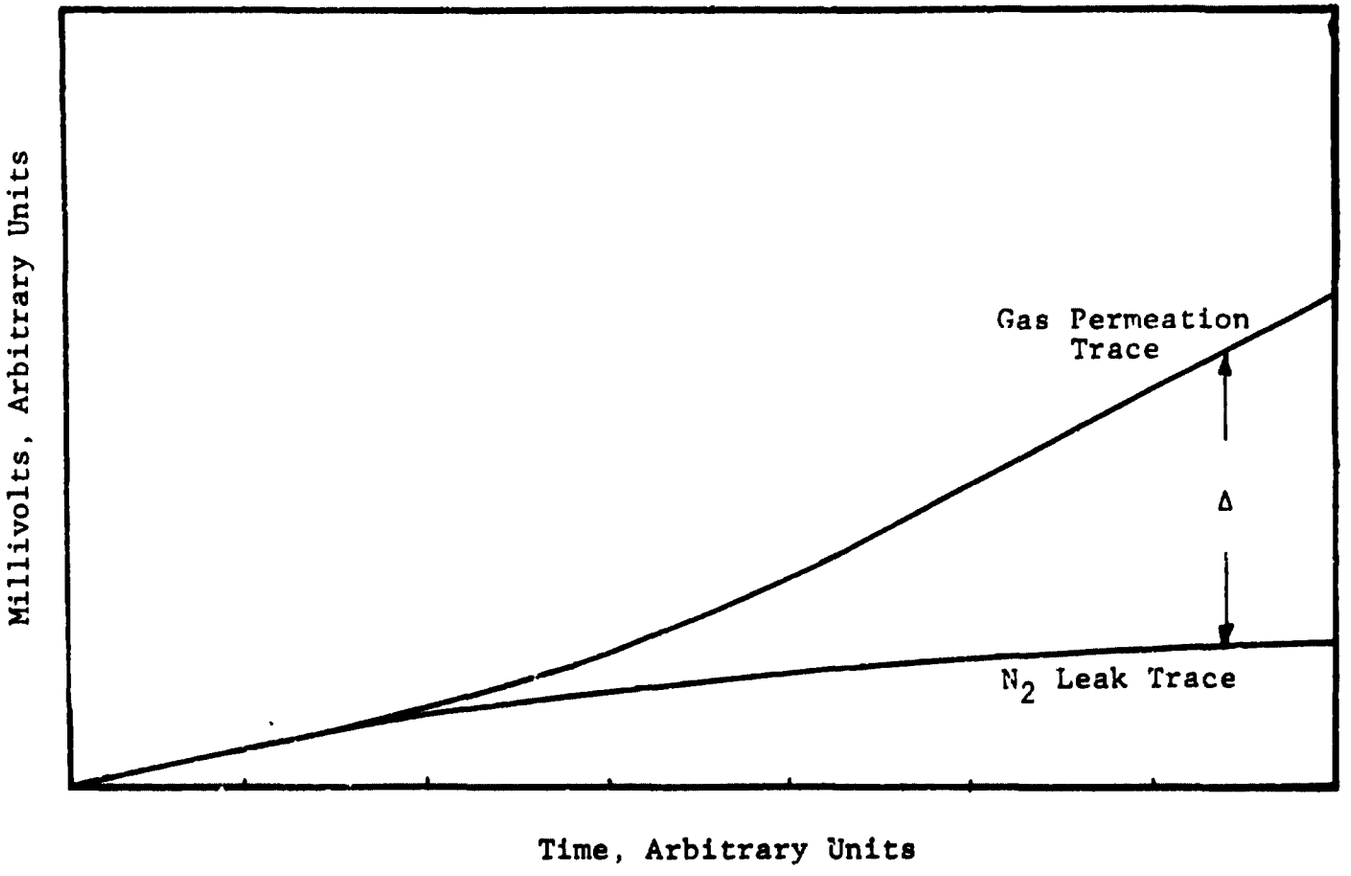

Figure 14

Schematic Representation of Nitrogen Leak and Permeation Traces of Chart Recorder. From the difference (Δ), the net permeation was estimated.

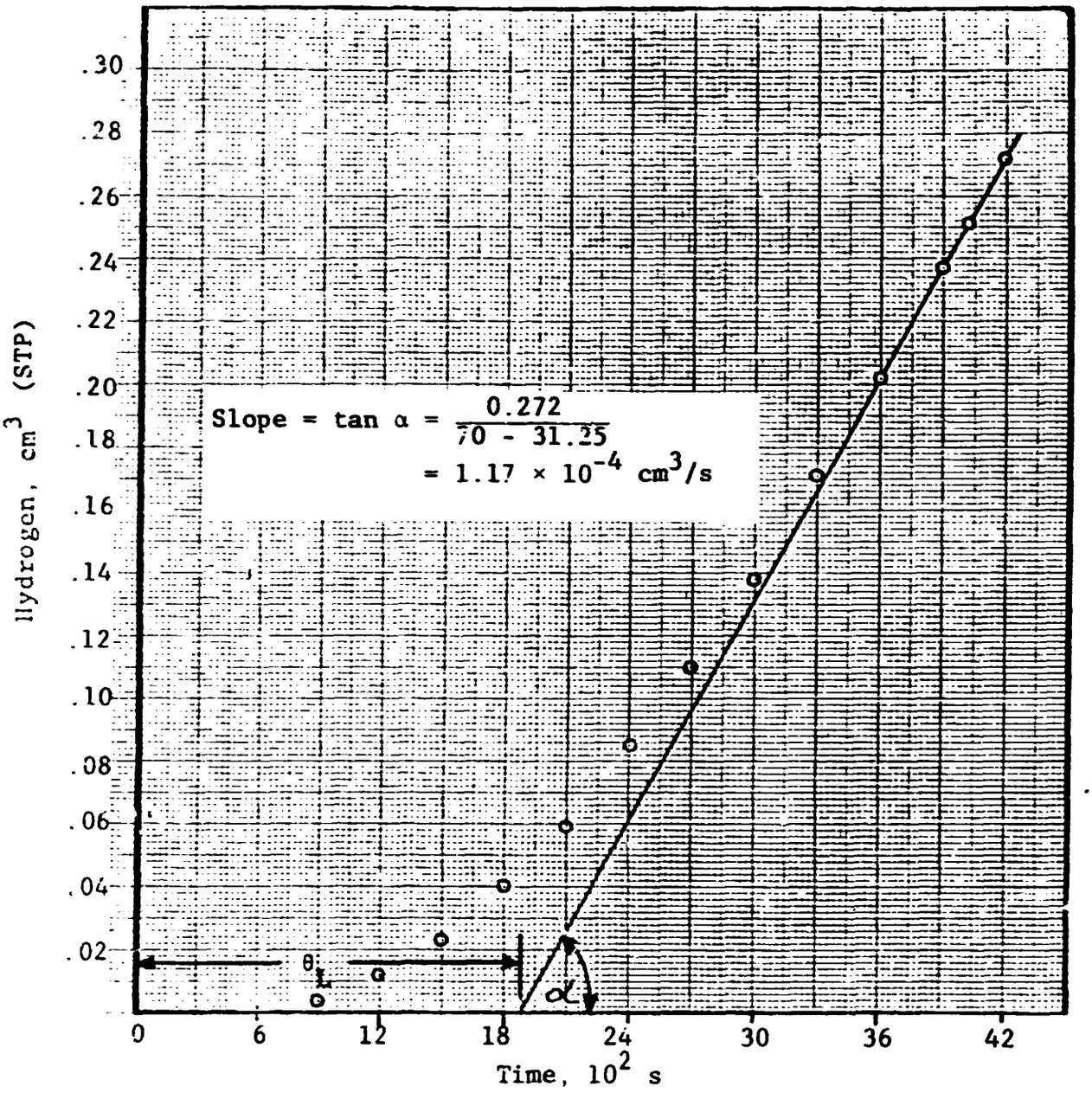

Figure 15

Amount of Hydrogen Permeation Versus Time,
Sample B2 (IN 800), 815°C

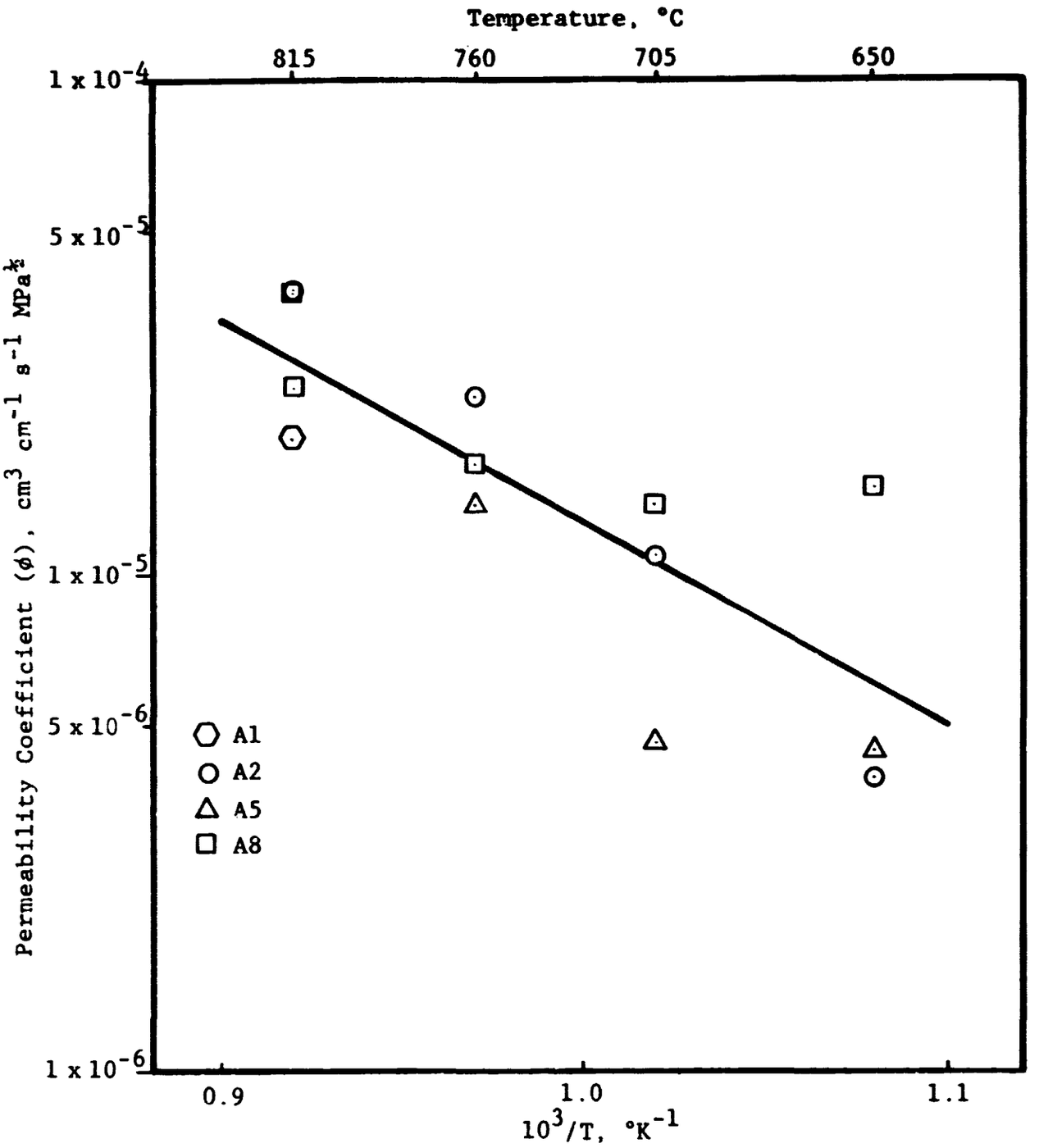

Figure 16

Effect of Temperature on the Permeability Coefficient of N-155

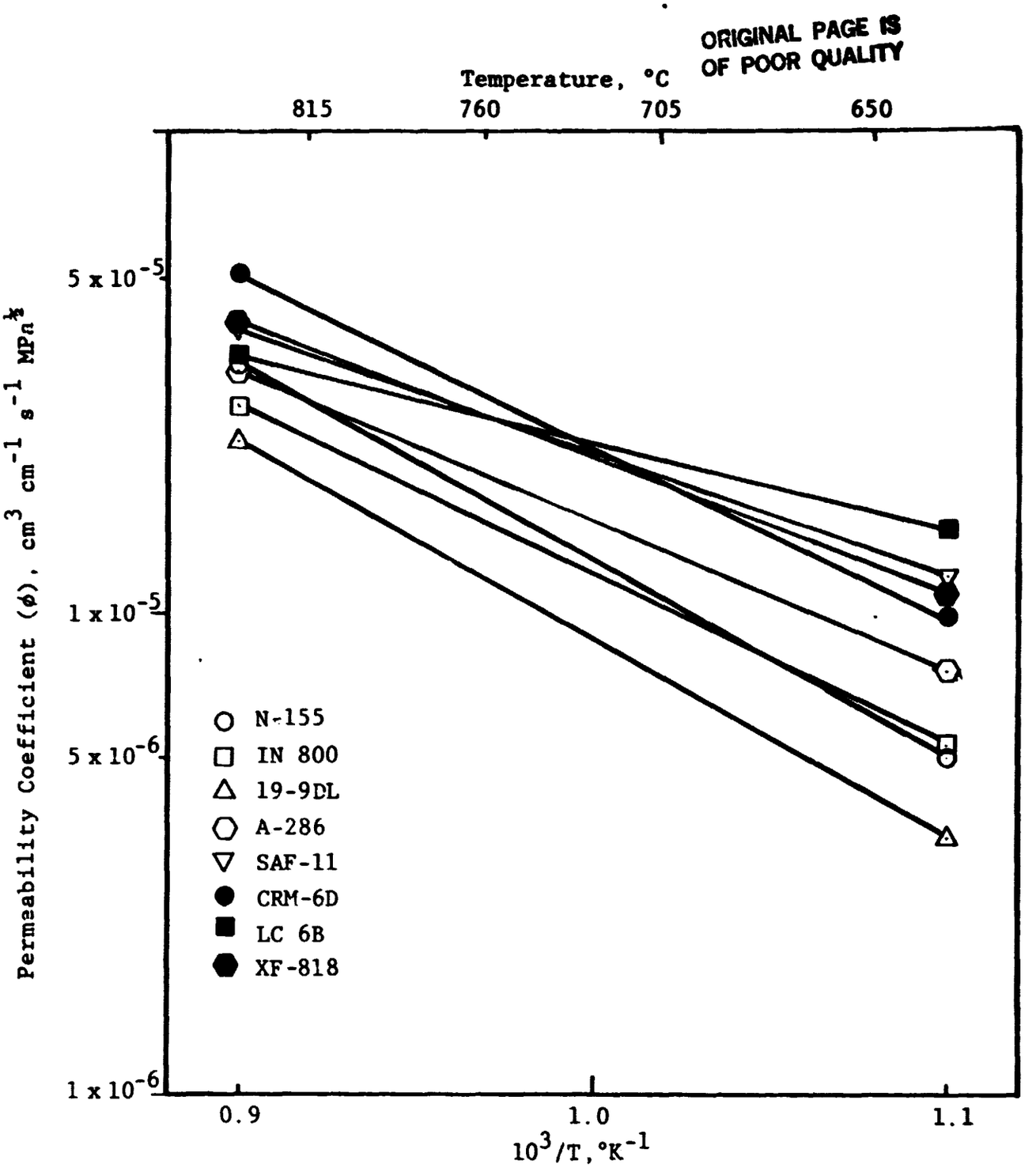

Figure 17

Effect of Temperature on Permeability Coefficient of Iron- and Cobalt-Base Alloys for the Range 650°-815°C

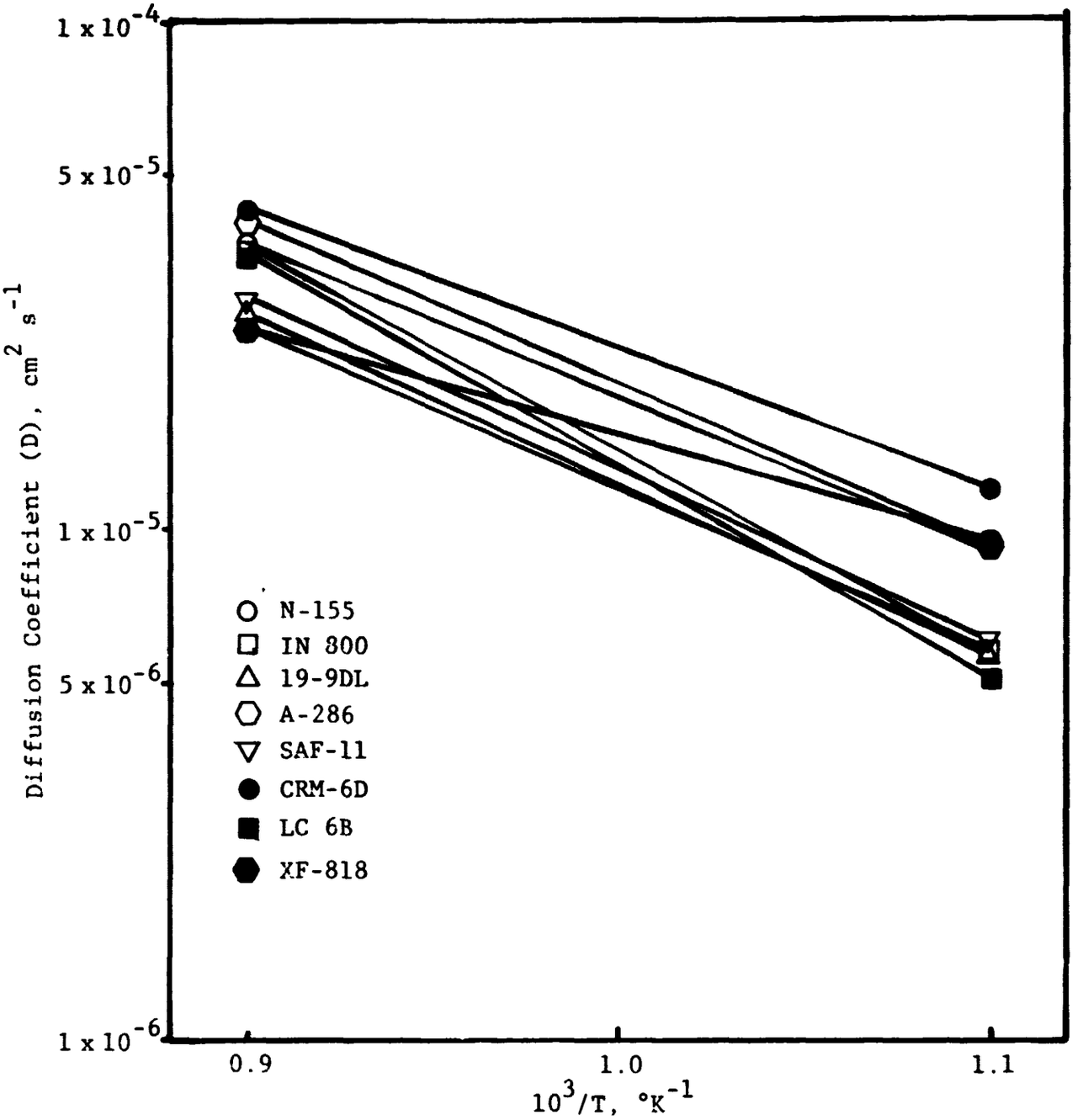

Figure 18

Effect of Temperature on Diffusion Coefficient of Iron- and Cobalt-Base Alloys for the Range 650°-815°C

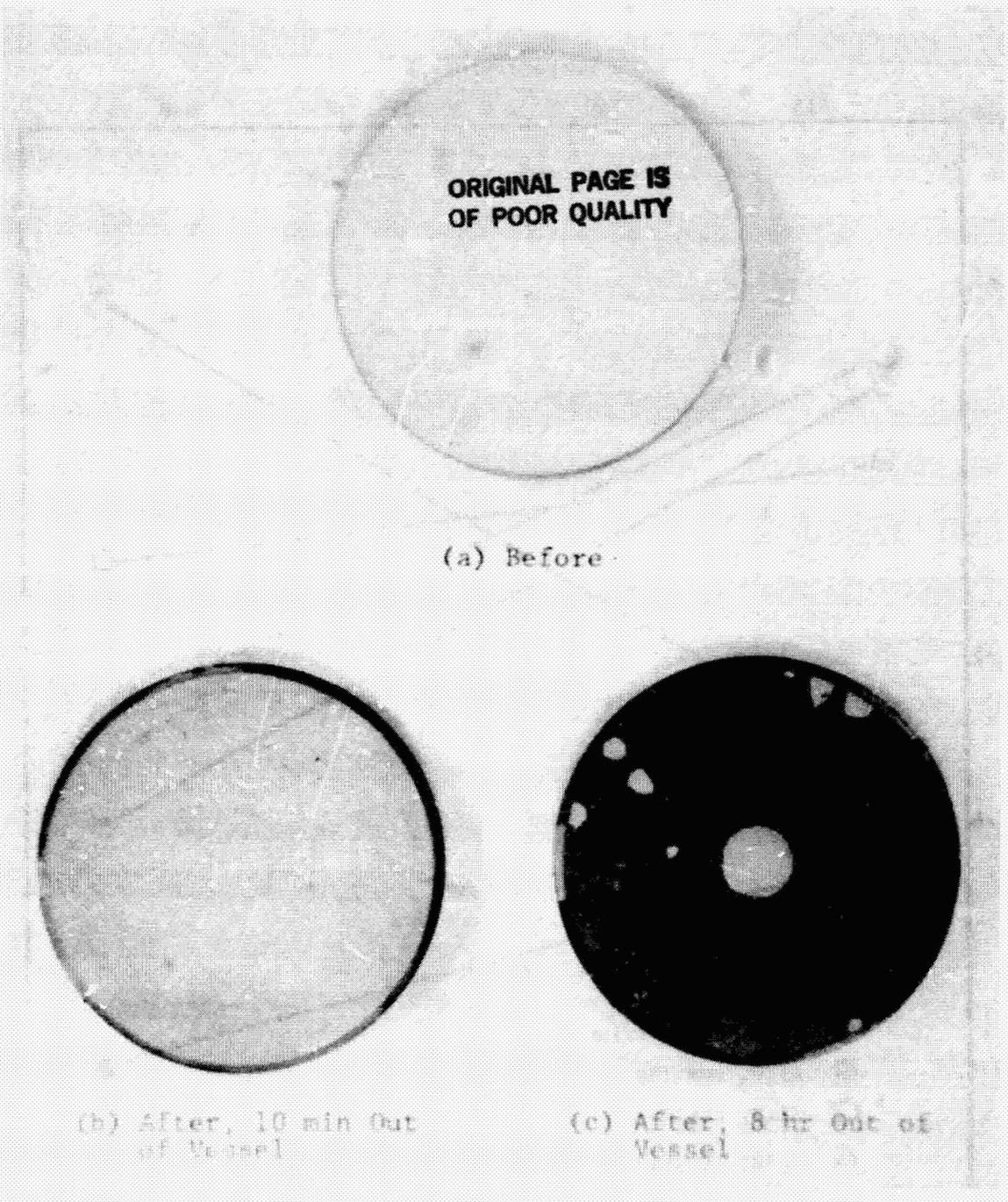

Figure 19

Surface Appearance of Al_2O_3-Coated N-155 Specimens Before and After Testing

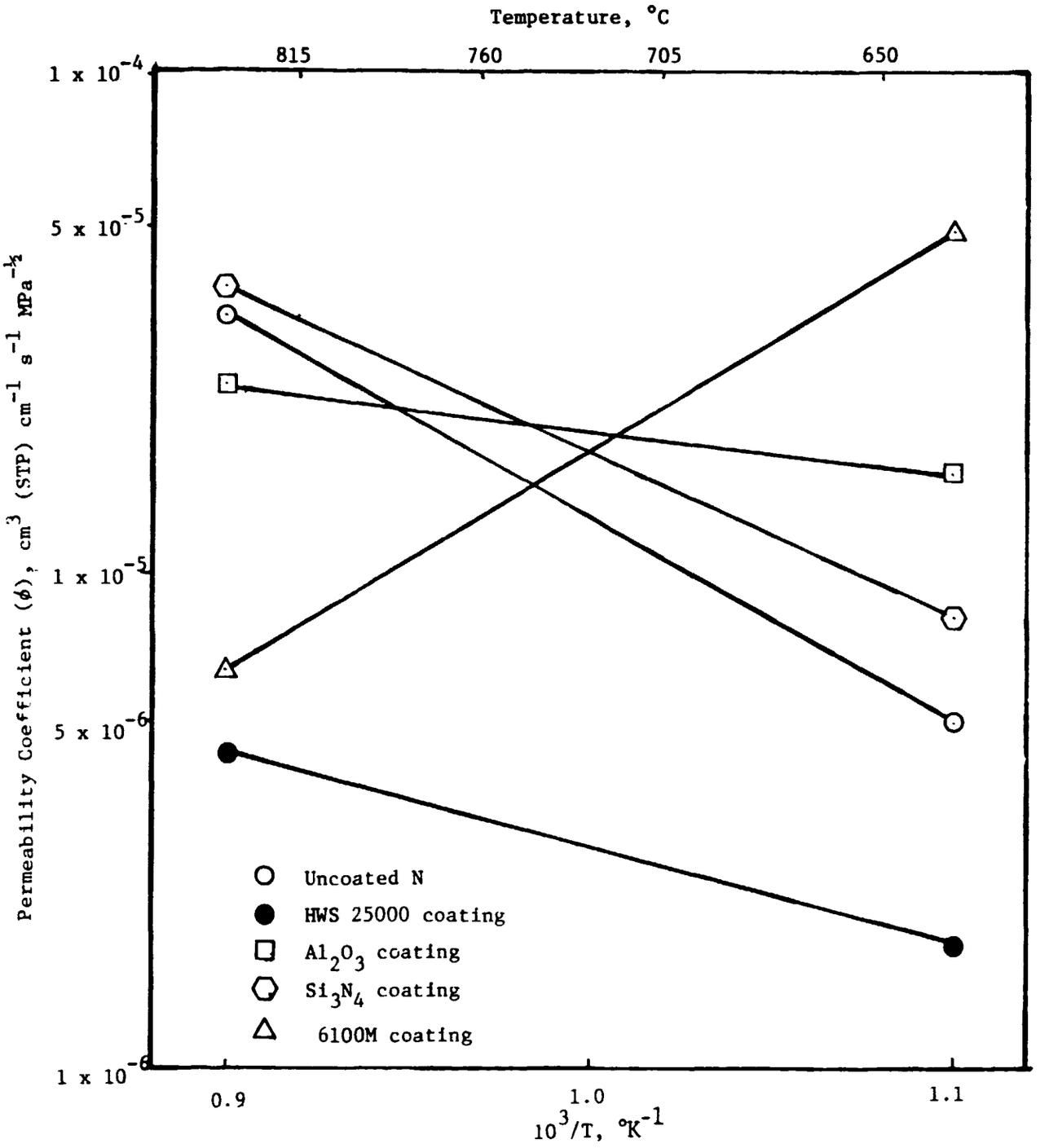

Figure 20

Effect of Temperature on Hydrogen Permeability
for Different Coatings Applied to N-155

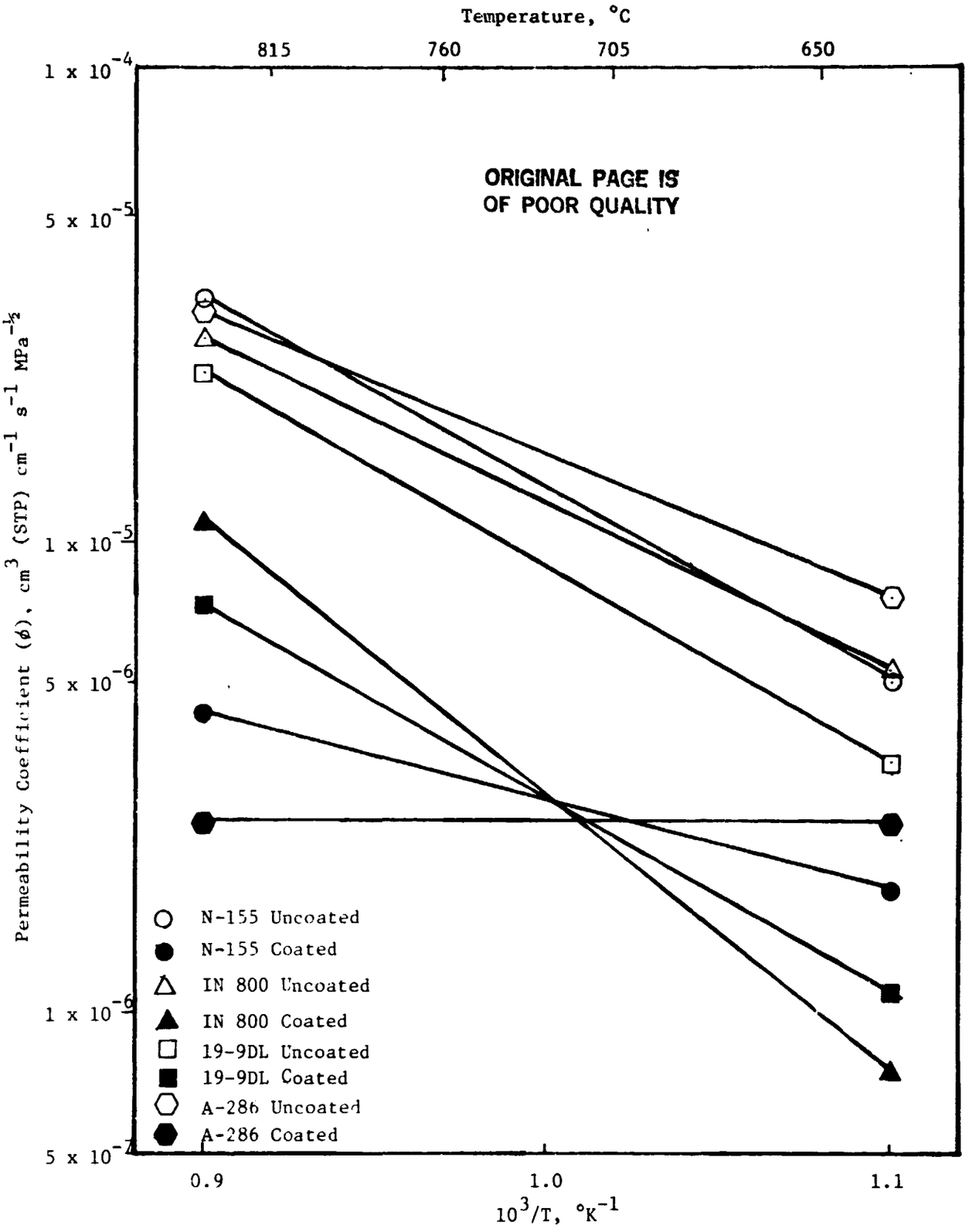

Figure 21

Effect of Temperature on Hydrogen Permeability Coefficient in HWS 25000 Coated and Uncoated Iron-Base Alloys